



SOAR *TESS* Survey. I. Sculpting of *TESS* Planetary Systems by Stellar Companions

Carl Ziegler¹ , Andrei Tokovinin² , César Briceño², James Mang³, Nicholas Law⁴ , and Andrew W. Mann⁴ 

¹Dunlap Institute for Astronomy and Astrophysics, University of Toronto, 50 St. George Street, Toronto, ON M5S 3H4, Canada; carl.ziegler@dunlap.utoronto.ca
²Cerro Tololo Inter-American Observatory, Casilla 603, La Serena, Chile

³Department of Astronomy, University of California, Berkeley, 510 Campbell Hall, Berkeley, CA 94720, USA

⁴Department of Physics and Astronomy, The University of North Carolina at Chapel Hill, Chapel Hill, NC 27599-3255, USA

Received 2019 August 28; revised 2019 October 30; accepted 2019 November 9; published 2019 December 17

Abstract

The *Transiting Exoplanet Survey Satellite* (*TESS*) is finding transiting planet candidates around bright, nearby stars across the entire sky. The large field of view, however, results in low spatial resolution; therefore, multiple stars contribute to almost every *TESS* light curve. High angular resolution imaging can detect the previously unknown companions to planetary candidate hosts that dilute the transit depths, lead to host star ambiguity, and, in some cases, are the source of false-positive transit signals. We use speckle imaging on the Southern Astrophysical Research (SOAR) telescope to search for companions to 542 *TESS* planet candidate hosts in the southern sky. We provide correction factors for the 117 systems with resolved companions due to photometric contamination. The contamination in *TESS* due to close binaries is similar to that found in surveys of *Kepler* planet candidates. For the solar-type population, we find a deep deficit of close binary systems with projected stellar separations less than 100 au among planet candidate hosts (44 observed binaries compared to 124 expected based on field binary statistics). The close binary suppression among *TESS* planet candidate hosts is similar to that seen for the more distant *Kepler* population. We also find a large surplus of *TESS* planet candidates in wide binary systems detected in both SOAR and *Gaia* DR2 (119 observed binaries compared to 77 expected). These wide binaries almost exclusively host giant planets, however, suggesting that orbital migration caused by perturbations from the stellar companion may lead to planet–planet scattering and suppress the population of small planets in wide binaries. Both trends are also apparent in the M dwarf planet candidate hosts.

Unified Astronomy Thesaurus concepts: Exoplanets (498); Exoplanet formation (492); Binary stars (154); Close binary stars (254); Speckle interferometry (1552)

Supporting material: machine-readable tables

1. Introduction

Over decade-long primary and extended missions, the *Kepler* telescope (Borucki et al. 2010) detected the majority of known exoplanets. *Kepler* probed the large (Howard et al. 2012) and diverse (Lissauer et al. 2011; Welsh et al. 2012) Galactic population of planetary systems but only looked at relatively small regions of the sky at a time. Also, the observed stars in the prime mission were generally too distant for precision follow-up observations.

Beginning in 2018 July, the *Transiting Exoplanet Survey Satellite* (*TESS*; Ricker et al. 2014) searched the southern sky for exoplanets around nearby stars. These typically bright targets are accessible to measurements of planet masses with precision radial velocity and atmospheric characterization of planets with transmission spectroscopy. Several planets around bright stars have been confirmed (Huang et al. 2018; Dragomir et al. 2019; Vanderburg et al. 2019), with hundreds of additional candidates awaiting follow-up observations.⁵

The simultaneous field of view required for *TESS* is large, approximately 6% of the entire sky, which it covers with a relatively coarse pixel scale of $21'' \text{ pixel}^{-1}$. For reference, each *TESS* pixel subtends a region of the sky approximately $25\times$ that of each *Kepler* pixel. Each *TESS* pixel observes the flux made up of the blended contributions of multiple sources. The *TESS* Input Catalog (TIC; Stassun et al. 2018; Stassun et al. 2019) determined the contamination from known point

sources in two catalogs (APASS and 2MASS) likely to be in the *TESS* aperture for 3.8 million stars. While these catalogs' limiting magnitudes are relatively faint compared to the typically bright *TESS* targets ($T_{\text{mag,limiting}} \sim 17\text{--}19$), they are based on seeing-limited observations and not sensitive to binaries with separations less than $1''\text{--}2''$. Likewise, *Gaia* DR2 generally does not recover binaries with separations of less than $\sim 0.7''$, in particular nearby bright stars (Ziegler et al. 2018a).

High-resolution imaging has proven to be critical to confirm and characterize transiting planet candidates. Half of the solar-type stars (Raghavan et al. 2010) and a quarter of the M dwarfs (Winters et al. 2019) are found in multiple systems. The maximum of the distribution of orbital separations (~ 50 au for a solar-type binary and 20 au for M dwarfs) at a typical distance to a *TESS* host star of approximately 100 pc peaks at angular separations of $0.2''\text{--}0.5''$, accessible only by high angular resolution imaging. Therefore, most contamination from binary systems is not accounted for in the TIC.

For *Kepler*, the planet radius estimates for stars with detected companions increased by a factor of 1.6, on average (Ciardi et al. 2015; Ziegler et al. 2018b). In many cases, the identity of the planetary host star may be ambiguous, leading to two different possible radius estimates based on either scenario. In addition, the absence of companions can be used to rule out many common false-positive scenarios, allowing planets to be statistically validated (Morton & Johnson 2011; Torres et al. 2011).

The number of planet candidates detected by *Kepler* and currently by *TESS* outstrips the resources available on

⁵ <https://tess.mit.edu/alerts/>

conventional high-resolution instruments, such as laser guide star adaptive optics (AO).⁶ A useful strategy with *Kepler* was to perform a broad survey with a visible-light high-resolution instrument on a moderately sized telescope. These observations are able to find the majority of both physically bound companions and low-contrast asterisms that significantly alter the radius estimate of the planet candidate. The Robo-AO *Kepler* survey (Law et al. 2014; Baranec et al. 2016; Ziegler et al. 2017) observed 3857 planet candidate host stars with a laser-assisted AO robotic instrument on a 2 m class telescope (Baranec et al. 2014). The discoveries of companions corrected the radius estimates for 814 planet candidates (Ziegler et al. 2018b), contributed to the validation of over 1000 *Kepler* planets (Morton et al. 2016), and informed future observations with large-aperture telescopes. Six years after the *Kepler* prime mission ended, over half of the *Kepler* planet candidates had only been imaged at high resolution by Robo-AO.

The *TESS* sample can largely be covered by speckle interferometry due to host stars that are, on average, several magnitudes brighter than *Kepler*. Speckle interferometry on the Southern Astrophysical Research (SOAR) telescope has been developed and optimized over the past decade, and at present, it can image up to 300 targets a night with diffraction-limited resolution (Tokovinin 2018). Mann et al. (2019) found the astrometric precision of SOAR speckle imaging to be among the best compared to similar nonfixed high-resolution instruments. Imaging in Cousins *I* band, at the center of the *TESS* bandpass, can accurately determine the transit dilution in the *TESS* light curves due to detected companions, used to correct the planetary radius estimates.

Theory suggests that the presence of a nearby stellar companion can have a dire impact on the formation of circumstellar planetary systems: stirring planetesimals (Quintana et al. 2007), perturbing orbits resulting in high-eccentricity tidal migration (Naoz et al. 2012), truncating protoplanetary disks and shortening their lifetime (Jang-Condell et al. 2008; Kraus et al. 2012), and increasing photoevaporation (Alexander 2012). Ngo et al. (2016) found that hot Jupiters have significantly fewer companions at close separations compared to field stars but many more at wider separations. This suggests that these hot Jupiters may have been driven inward to their present few-day orbits by perturbations from the companion stars. Bolstering this interpretation, the Robo-AO *Kepler* survey found that hot Jupiters were significantly more likely to be found in binary systems than other types of planets (Ziegler et al. 2018c). Deacon et al. (2016), however, found no difference in the wide ($\rho > 3000$ au) binary rate between transiting planet hosts and field stars in the *Kepler* field.

Kraus et al. (2016), observing 382 *Kepler* planet candidates with AO on Keck, found a dearth of *Kepler* planets in close binary systems. This deficit was modeled as a binary suppression factor of 0.34 at separations below approximately 47 au. Extrapolating this out suggests that one-fifth of the solar-type stars in the galaxy cannot host planets due to the influence of a stellar companion. It is unclear, however, if the survival of planets in close binary systems is random or a result of other factors, such as the binary eccentricity or the mutual inclination to the planetary system of the binary system. The detection image provides only an instantaneous projected separation, s .

Further monitoring is needed to determine the true orbital parameters that could provide insight into how some planetary systems form and survive in this harsh environment.

The *TESS* planet candidate hosts are relatively nearby: on average, less than half the distance of the *Kepler* hosts, based on the TIC distance estimates (Stassun et al. 2019). The 4.1 m SOAR telescope can, therefore, detect companions to the vast majority of *TESS* targets at solar system separations ($s = 10\text{--}50$ au). Evidence of suppression in the binary rate for *TESS* planet candidates in this regime would serve as both an independent validation of the ruinous effect binaries have on planetary systems and, since the *TESS* planets are spread over the entire sky, confirmation of the effect in a more representative sample of the Galactic planetary population. Indeed, Matson et al. (2018) did not detect binary suppression in a sample of K2 stars, which are spread in fields across the ecliptic plane. The authors note that the nondetection is tenuous, however, and more high-resolution observations of exoplanet hosts are needed.

We begin in Section 2 by detailing our observations and data analysis. We present the results of the survey in Section 3 and explore the impact binaries have on the *TESS* planets in Section 4. We discuss the results further in Section 5. Finally, we conclude in Section 6.

2. Observations and Analysis

2.1. Target Selection

The hosts of *TESS* planet candidates (*TESS* objects of interest, or TOIs) were selected from the data releases available online at the *TESS* data release portal.⁷ Faint stars (typically, $T_{\text{mag}} > 13$ mag) that are not well suited for speckle observations were not targeted; this limit reduces the number of late-type stars that are observed in this survey. Previously confirmed planet hosts, primarily from the WASP (Street et al. 2003) and HATS (Bakos 2018) surveys, were excluded from the target selection, as these systems have been heavily studied in the past (e.g., Ngo et al. 2015; Evans et al. 2016, 2018). Seventeen community-detected *TESS* planet candidates⁸ were also observed but were not used in the subsequent analysis in this work. To increase observing efficiency, target acquisition was improved using precise target coordinates, determined for each night with proper motions from *Gaia* DR2 (Gaia Collaboration et al. 2018), when available, and the TIC (Stassun et al. 2019) otherwise. As previously noted in Arenou et al. (2018), we find that many targets with only two-parameter astrometric solutions in *Gaia* DR2 are actually close binaries.

The properties of the host stars and planet candidates observed are plotted in Figure 1.

2.2. SOAR Observations and Data Reduction

We observed 542 *TESS* planet candidate hosts with the high-resolution camera (HRCam) imager on the 4.1 m SOAR telescope over 7 nights in 2018–2019. The observation procedure and data reduction are described in Tokovinin (2018). Briefly, each observation consists of 400 frames split into two data cubes, typically consisting of a 200×200 binned pixels region of interest centered on the target star ($6''3$ on a

⁶ For example, the acquisition time of Keck-AO averages 9 minutes (Wizinowich et al. 2006), so over 100 nights would be needed to observe the *Kepler* planet candidates.

⁷ <https://tev.mit.edu/toi/> (account required for access).

⁸ From the CTOI list, available at https://exofop.ipac.caltech.edu/teess/view_ctoi.php.

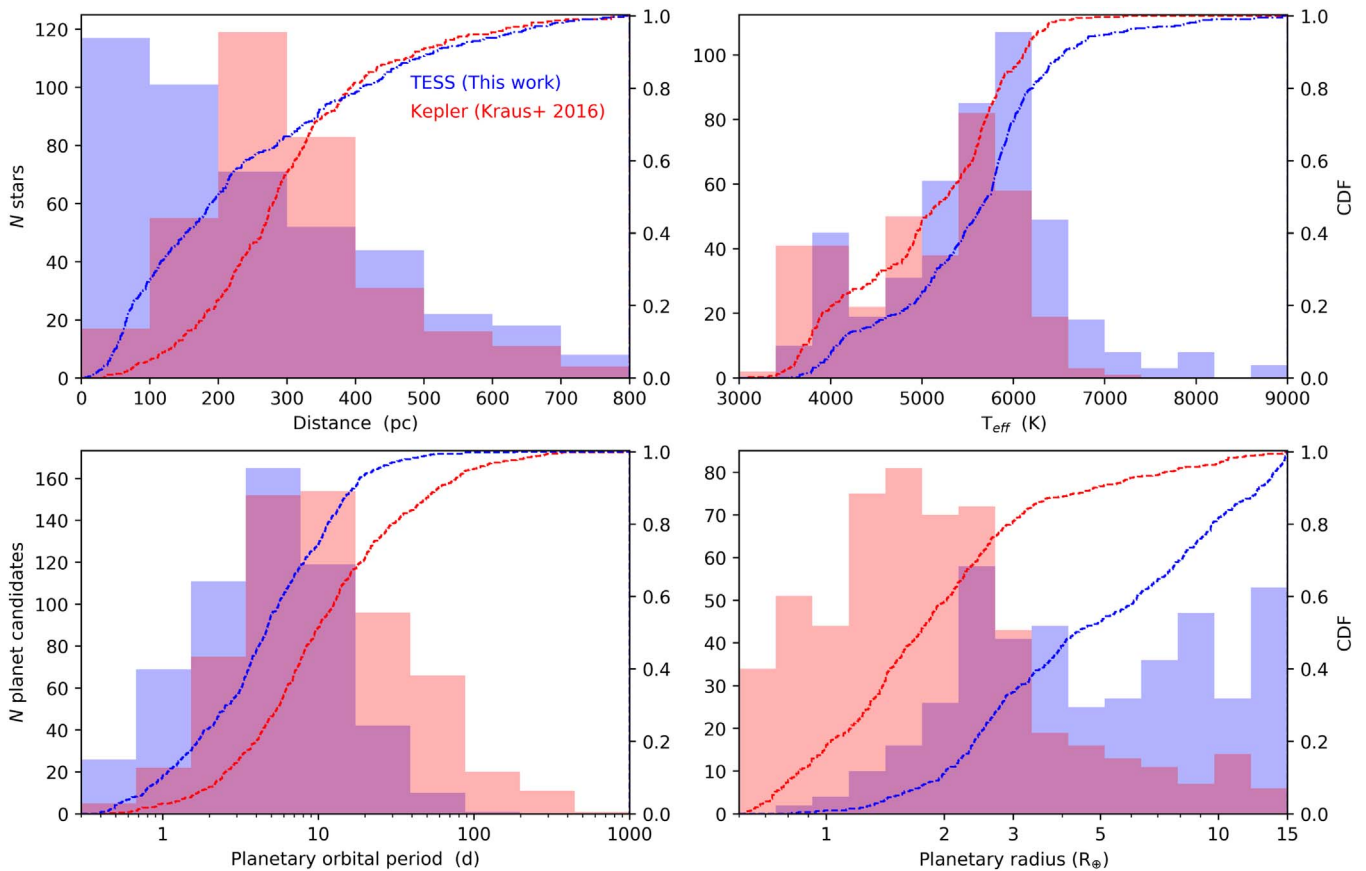


Figure 1. Properties of the 542 *TESS* planet candidate hosts observed by SOAR in this survey, presented as a binned histogram with an overplotted cumulative density function. For comparison, the properties of the 382 *Kepler* planet candidate hosts observed in Kraus et al. (2016) are also plotted. In general, the *TESS* planets are closer to the solar system, have slightly hotter hosts, orbit with shorter periods, and are larger than the *Kepler* planets targeted by the Kraus et al. (2016) survey.

side at the pixel scale of $0''.01575$ and 2×2 binning) taken in approximately 11 s with an Andor iXon-888 camera. The resulting data cube is processed by a custom IDL script, which computes the power spectrum, in which a resolved multiple stellar system will appear as characteristic fringes. Binary parameters (separation, position angle, and magnitude difference) are determined from modeling the power spectrum. Secondary stars will appear as mirrored peaks in the speckle autocorrelation function (ACF), the Fourier transform of the power spectrum, at the separation and position angle of the companion. To remove the 180° ambiguity inherent to the classical speckle interferometry, our pipeline also computes the shift-and-add (SAA) images, centered on the brightest pixel in each frame (this is sometimes called “lucky imaging”). Relatively bright binaries with $\Delta m > 0.5$ mag often have their companions visible in the SAA images, allowing us to select the correct quadrant (these measurements are marked by the flag “q” in Table 6 in the Appendix). In all other cases, the position angles are determined with a 180° ambiguity. Figure 4 in Tokovinin (2018) gives an example of typical speckle data, including the SAA image. Observations were taken in the *I* band ($\lambda_{\text{cen}} = 824$ nm, $\Delta\lambda = 170$ nm), which is approximately centered on the *TESS* bandpass. Four resolved systems (TOI 123, 131, 138, and 146) were also imaged in the *V* band in preparation for a future association analysis.

The detection limits are estimated from the rms fluctuations σ of the ACF computed in annular zones of increasing radii; peaks exceeding the 5σ level are assumed to be detectable. This

has been verified by injecting simulated binary companions into the real ACFs (see, e.g., Figure 9 in Tokovinin et al. 2010). Moreover, for each target, we require detection of the companion in both data cubes. Our procedure practically excludes false detections at separations larger than $\sim 0''.1$. At closer separations, however, the faint and persistent ACF details of instrumental origin, such as vibration or the optical ghosts described in Tokovinin (2018), can mimic real close binaries with a large Δm . We intercompare the ACFs and power spectra of sequentially observed targets to identify such artifacts. Finally, the estimated detection limits are verified by comparing with the $(\rho, \Delta m)$ of actually measured companions, and a good agreement is always found.

The pixel scale and orientation are calibrated by observing several wide binaries with a well-modeled motion, as explained in Section 4.2 of Tokovinin (2018). The rms agreement between the measured calibrator positions and their models is typically from 1 to 3 mas in separation and better than $0''.2$ in angle. The pixel scale is therefore established with an accuracy of better than 0.5%. The calibration of HRCam was checked by comparing the positions of wider calibrators predicted by their models for 2015.5 with their relative positions in *Gaia* DR2.

We detail the observations in Table 6 in the Appendix. The cumulative 5σ detection sensitivities are plotted in Figure 2.

2.3. Planet Radius Corrections

The additional flux from a nearby star will dilute the transit depth in the *TESS* light curves, resulting in an underestimated

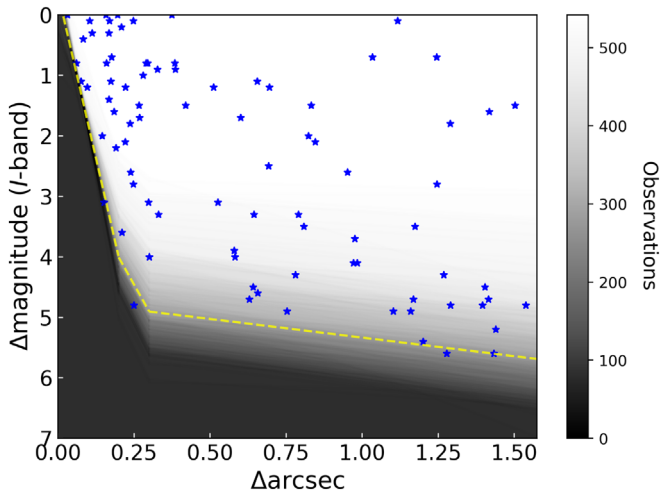


Figure 2. Close companions ($\rho < 1''.55$) to the *TESS* planet candidate hosts detected by SOAR speckle imaging, in terms of their *I*-band magnitude difference and separation from the primary star. The average 5σ detection limits of the observations are plotted, trending from black (no observations are sensitive to binaries with that combination of separation and contrast) to white (all 542 observations are sensitive to that combination). The yellow dashed line shows the median sensitivity for the survey.

radius for the planet candidate. We compute correction factors to the radius estimates derived from the *TESS* light curves for two scenarios: (1) the planet orbits the target star and (2) the planet orbits the secondary star, which is bound to the primary star.⁹

For the first scenario, we use the relation from Law et al. (2014) to derive a radius correction factor,

$$X_{\text{prim}} = \frac{R_{p,A}}{R_{p,0}} = \sqrt{\frac{1}{F_A}}, \quad (1)$$

where $R_{p,A}$ is the corrected radius of the planet orbiting the primary star, $R_{p,0}$ is the original planetary radius estimate based on the diluted transit signal, and F_A is the fraction of flux within the aperture from the primary star.

For the case where the planet candidate is bound to the secondary star, we use the relation for the radius correction factor,

$$X_{\text{sec}} = \frac{R_{p,B}}{R_{p,0}} = \frac{R_B}{R_A} \sqrt{\frac{1}{F_B}}, \quad (2)$$

where $R_{p,B}$ is the corrected radius of the planet orbiting the secondary star bound to the primary star; R_B and R_A are the stellar radii of the secondary and primary star, respectively; and F_B is the fraction of flux within the aperture from the secondary star.

We use the stellar radius estimates from the TIC (Stassun et al. 2019) when available for the primary stars. The radii of secondary companions in the scenario where they are bound to the target star were estimated using the observed contrast ratio in the *TESS* band (approximated using the *I* bandpass of SOAR) and finding the radius of an appropriately fainter star within the Dartmouth stellar models (Dotter et al. 2008).

⁹ A third scenario, in which the secondary star is unbound to the primary star, is unconstrained without color information. In future papers, we will use multiband speckle imaging with SOAR to extend our analysis to the unbound scenario.

The TIC includes a contamination ratio that takes into account stars within 10 *TESS* pixels of the target. This includes stars typically down to the limiting magnitude of the 2MASS (Skrutskie et al. 2006) and APASS (Henden et al. 2009) catalogs ($T \sim 17$ – 19). Using the list of detected close binaries to *TESS* planet candidate hosts and their binary parameters, a custom Python script crossmatched each of their coordinates to stars in the TIC catalog. We find that 31 stars in the TIC had similar positions relative to the primary as was found in SOAR imaging ($\Delta\rho < 0''.5$ and $\Delta\theta < 20^\circ$, or $[\Delta\theta \pm 180^\circ] < 20^\circ$). The properties of these systems are available in Table 2 in the Appendix. One notable resolved binary in our survey is the pair TOI 658 and TOI 659. The magnitude differences in the *TESS* bandpass for wide binaries in the TIC are generally similar to that measured from the SOAR observations, supporting our use of *I*-band observations as a proxy for the *TESS* observations. A similar crossmatch was performed with *Gaia* DR2 (Gaia Collaboration et al. 2018), yielding 38 matches to SOAR detected companions. These companions were all widely separated ($\rho > 1''$). The separations measured by SOAR have a mean and median difference of 15 and 6 mas, respectively, compared to those reported in *Gaia* DR2. The average difference in magnitude differences between SOAR and *Gaia* DR2 is 0.16 mag and likely due to the different passbands. The properties of these systems are available in Table 4 in the Appendix.

We provide a correction factor for hosts, as in some cases the crossmatch between the TIC and the SOAR binary is ambiguous; however, we caution that the correction should be used judiciously. For all other systems, the contamination ratios reported should be used in addition to the TIC contamination ratio. In practice, the reported radius estimates of *TESS* planet candidates on the *TESS* data release portal and Exoplanet Follow-up Observing Program (ExoFOP) typically take into account flux contamination. The additional correction due to binaries detected by SOAR is the product of the original radius estimate and the radius correction factor reported in this work.

2.4. Physical Association of Companions

A relatively large number of companions detected near *Kepler* planet candidates were unassociated, especially at separations greater than $1''$ (Horch et al. 2014; Ziegler et al. 2018c). The *TESS* targets are spread across the sky, in regions of low and high stellar density, but generally at higher Galactic latitudes than the *Kepler* field. In addition, the targets are typically bright ($T_{\text{mag}} < 12$ mag), and subsequently, the detectable stars near them are several magnitudes brighter than the *Kepler* stars, given approximately equal contrast sensitivity. It is likely, then, that the number of detected field stars will be reduced in the *TESS* sample.

We use the stellar densities in the region of sky around each target in *Gaia* DR2 (Gaia Collaboration et al. 2018) to estimate the likelihood of a field star being detected near a *TESS* star. *Gaia* DR2 is essentially complete for sources down to $G = 17$ mag, or $G = 19$ mag in noncrowded fields (Gaia Collaboration et al. 2018). For our typical target with $I = 12$ mag and a contrast sensitivity of 5 mag, the faintest detectable companions will have $I \approx 17$ mag, comparable to the *Gaia* completeness limit.

For each target, we begin by performing a cone search in DR2 to search for all stars within $0''.5$. The cone search was

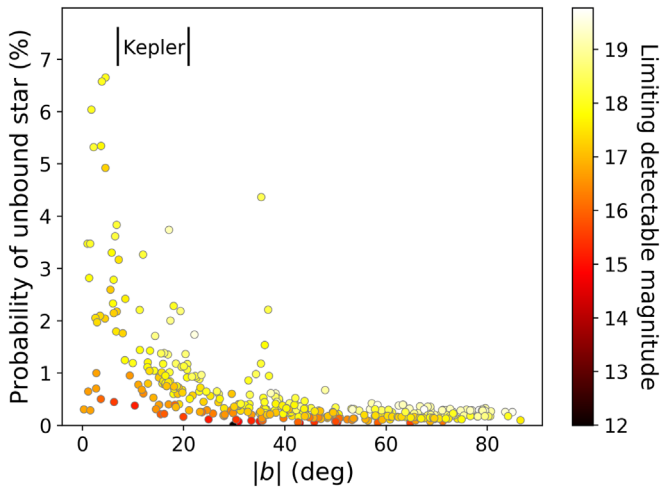


Figure 3. Probability of an unbound star being detected within the search radius of $3''/15$ for each observed *TESS* planet candidate as a function of Galactic latitude, based on *Gaia* DR2 stellar counts. Each target is colored by the limiting magnitude of detectable nearby stars in the SOAR speckle observations. The latitude range of the primary *Kepler* mission is indicated for reference. We expect approximately three unbound stars in total to be detected near the *TESS* planet candidates.

done using the Astropy affiliated package *astroquery* (Price-Whelan et al. 2018) to search the *Gaia* DR2 catalog hosted by the Barbara A. Mikulski Archive for Space Telescopes (MAST). We use the number of sources in DR2 within the 0.5 circular field to determine the source density (i.e., number of sources per arcsec^2) as a function of G magnitude, $\rho_{\text{source}}[G]$. For each target, we determine the limiting magnitude of detectable secondary stars (G_{limit}) within separation increments of $0''.5$. We then use these limiting magnitudes and the DR2 source density ($\rho_{\text{source}}[G < G_{\text{limit}}]$) to determine the probability of detecting an unassociated field star within that separation range (e.g., $1''-1''.5$). The cumulative probability for all separations out to $3''/15$ provides the number of field stars we can expect to find near that target (see Figure 3). Typically, targets near the galactic plane and the Small and Large Magellanic Clouds are far more likely to have a field companion due to the high local source density.

We perform a Monte Carlo analysis using these probabilities and the distribution of contrast sensitivity to simulate 10^4 surveys and find that, on average, we should detect 3.2 ± 0.5 field stars within $3''/15$ of the observed *TESS* targets. The field companions are nearly always high contrast (with a large ΔI). Therefore, we expect the impact on the subsequent analysis due to unassociated asterisms of field stars to be negligible.

3. Results

We detected 88 and 126 companions within $1''.5$ and $3''$ of 84 and 117 *TESS* planet candidate hosts, respectively, out of 542 observed with speckle imaging on SOAR. This implies a companion rate within $1''.5$ and $3''$ for *TESS* planet candidates of $16.2\% \pm 1.7\%$ and $23.2\% \pm 2.0\%$, respectively. The properties of the detected companions are plotted in Figure 2, along with the average detection sensitivities from all observations, which are detailed in Table 6 in the Appendix. We include the radius correction factors for planets in these systems, whether they orbit the primary or secondary star. The ACFs of resolved systems showing the position of the companions are shown in Figures 11–14 in the Appendix.

The results of each night’s observations were processed within a week and posted on the *TESS* ExoFOP website¹⁰ to aid in confirmation of the planet candidates. Several studies (Espinoza et al. 2019; Jones et al. 2019; Quinn et al. 2019; Rodriguez et al. 2019; Vanderburg et al. 2019) have used the SOAR speckle results to confirm early *TESS* planets.

3.1. High-order Multiples

Nine targets are resolved triples with two companions in the SOAR images. For TOIs 378, 183, 487, 952, and 909, both companions are paired to the main star. In contrast, close pairs in TOI 455, 697, and 612 belong to the secondary components. Finally, in TOI 141, both separations are comparable, $1''.2$ and $0''.44$. For the resolved triples, the positions and magnitude differences refer to pairs of stars (e.g., Aa,B and Aa,Ab), as indicated in Column 3 of Table 6 in the Appendix, not the merged inner pairs like A,B.

3.2. Implications for *TESS* Planet Radii

As discussed in Section 2.3, the additional flux from a stellar companion will dilute the transit signal in the *TESS* light curves, resulting in an underestimated planetary radius. We report the radius correction factors for planet candidates hosted in resolved binaries in our survey in Table 1.

In general, the identity of the host star for an S-type planet in a close binary is ambiguous (Horch et al. 2014), although there is evidence that typically, the primary is more likely to be the planet host (Gaidos et al. 2016). Therefore, we report correction factors for each host scenario. Overall, we find a mean correction factor of 1.11 in the cases where all of the planets orbit the primary stars. This is similar to the factor of 1.08 found for *Kepler* planets (Ziegler et al. 2018b) under the same assumption. Likewise, if all planets orbit the secondary stars that are bound to the primary,¹¹ the radii of the planets will increase by a factor of 2.55, on average. This is slightly less than the 3.29 found for *Kepler* planets by Ziegler et al. (2018b), which is likely due to the lower number of field stars detected in the *TESS* sample (see Section 2.4). Indeed, if a faint field companion is considered as bound, its estimated radius is small, and the resulting correction factor for the radius of a planet orbiting this companion becomes large.

In perhaps a more realistic scenario, where planets are equally likely to orbit the primary or secondary star, we find an average correction factor of 1.82. This again is slightly lower than the correction factor of 2.18 found with similar assumptions in the *Kepler* survey.

We can restrict our separation range to reduce the fraction of unassociated stars in our sample. Within $1''$, we find mean correction factors of 1.14, 1.90, and 1.55 under the assumptions that all primary stars host the planets, all secondary stars host the planets, and either star is equally likely to host the planet, respectively. The latter figure, more probable than either of the other cases, is in agreement with the radius corrections of 1.6, 1.64, and 1.54 found for the *Kepler* planets by Ciardi et al. (2015), Hirsch et al. (2017), and Ziegler et al. (2018b), respectively.

¹⁰ <https://exofop.ipac.caltech.edu/tess/>

¹¹ Not every *TESS* planet candidate host had stellar radius estimates in the TIC or *Gaia* DR2. These targets are only included in calculating the mean correction factors in the case in which the primary star is assumed to be the host. In this case, only the flux contribution of the primary star is needed to determine the correction factor, as seen in Equation (1).

Table 1
Nearby Stars Detected by SOAR to *TESS* Planet Candidate Hosts

TOI	Separation (arcsec)	P.A. (deg)	Contrast (<i>I</i> band)	T_{eff} (K)	Distance (pc)	Proj. Sep. (au)	Radius Correction Factor		Prev. Det.?	WDS DD
							(Primary Host)	(Secondary Host)		
1	2	3	4	5	6	7	8	9	10	11
123	1.2894	294.6	1.8	6188	72	92	1.091	2.404	3	SEE443
128	2.2195	153.8	2.4	6086	67	148	1.053	3.13	2	FIN92
131	0.0755	207.1	1.1	4174	55	4	1.168	1.932	1	
138	0.0964	257.0	1.2	5722	128	12	1.154	2.005	1	
141	1.1999	305.2	5.4	5795	48	57	1.003	10.881	1	
141	0.4429	239.5	4.9	5795	48	21	1.005	8.66	1	
146	0.2896	76.1	0.8	6905			1.216		1	
147	2.6583	217.6	4.6	5620	820	2179	1.007		3	
149	1.117	132.6	0.1	5914	376	419	1.383		3	TDS161
153	0.1691	173.6	0.1	6142	436	73	1.383	1.425	1	
159	0.6444	17.5	3.3	6979	333	214	1.024	4.594	1	
161	0.1961	101.2	0.0	5388	333	65	1.414	1.414	1	
165	2.4855	254.5	0.8	6038	193	479	1.216	1.686	2	RST164
167	0.1593	306.6	0.8	5551	293	46	1.216	1.776	3	
172	1.1021	319.1	4.9	5911	225	247	1.005	9.603	1	
180	1.2682	63.7	4.3	6082	270	342	1.009	7.197	3	
183	0.083	98.5	0.4	6270	200	16	1.301	1.495	1	
183	3.1806	302.0	5.1	6270	200	636	1.005	10.056	1	
187	0.8456	104.5	2.1	6725	177	149	1.07	2.797	1	
188	1.2904	5.8	4.8	6340	203	261	1.006	8.547	1	
189	0.9716	341.7	4.1	6054	177	171	1.011	6.411	1	
211	0.2083	258.3	0.2	5873	121	25	1.353	1.338	1	
224	0.0607	31.1	0.8	3689	64	3	1.216	1.63	1	
235	0.8326	291.6	1.5	5454	104	86	1.119	2.151	2	B2080
240	2.3656	197.6	3.1	4333	74	175	1.028	4.128	3	
242	0.8233	164.3	2.0	6083	589	484	1.076	2.66	1	
245	1.6268	258.2	1.7	6208	126	204	1.1	2.313	2	B584
252	0.4192	311.5	1.5	5071	190	79	1.119	2.105	1	
253	2.6623	351.2	4.0	4020	30	79	1.012	5.734	3	
258	2.0749	343.2	2.9	6474	561	1164	1.034	3.662	3	
264	0.6413	331.5	4.5	5773	422	270	1.008	7.22	1	
268	2.3025	51.2	0.3	5868	305	702	1.326	1.373	2	HU1368
293	0.7905	0.3	3.3	5817	313	247	1.024	4.22	1	
295	0.9838	151.8	4.1	5663	389	382	1.011	6.656	1	
308	0.1576	45.2	0.0	4416	201	31	1.414		1	
309	0.3266	77.9	0.9	5312	345	112	1.199	1.692	1	
322	0.1761	126.5	0.7	5868	277	48	1.235	1.537	1	
325	0.5815	222.2	4.0	4275	180	104	1.012		1	
337	0.1451	60.8	2.0	5369	292	42	1.076	2.606	1	
340	0.237	338.0	1.8	5655	497	117	1.091	2.39	1	
343	2.8471	321.0	4.5	5695	438	1247	1.008	7.817	3	
346	1.4329	285.3	5.6	5835	745	1067	1.003		1	
348	1.3959	40.8	4.8	5714	420	586	1.006	8.958	1	
364	0.3739	96.1	0.0	6219	265	99	1.414	1.414	1	
369	0.6949	139.4	1.2	6228	126	87	1.154		2	B600
372	0.2386	260.6	2.6	5400	340	81	1.045	3.334	1	
378	0.1839	330.0	1.6	5894	629	115	1.109	2.316	1	
378	3.3108	312.3	1.5	5894	629	2082	1.119	2.232	1	
379	0.031	28.8	0.0	5895	227	7	1.414	1.414	1	
383	0.2665	333.6	1.5	5951	204	54	1.119	2.118	1	
386	1.1739	274.4	3.5	8100	452	530	1.02	5.111	3	
387	2.2878	342.9	3.2	6191	193	441	1.026	4.306	3	
394	3.2284	220.2	3.8	6329	149	481	1.015	5.583	2	BU529
402	1.4388	233.4	5.2	5175	44	63	1.004	10.825	1	
405	0.3856	321.5	0.9	6138	266	102	1.199	1.785	1	
409	3.2443	20.4	5.2	4986	53	171	1.004	10.819	1	
415	2.2303	89.6	4.8	6471	381	849	1.006	8.547	1	
422	1.4038	118.8	4.5	5823	98	137	1.008	7.22	1	
427	2.6122	152.9	4.8	5409	145	378	1.006	8.843	1	
433	4.0098	324.5	2.9	8543	498	1996	1.034	3.795	3	A3013
454	3.8682	256.7	2.2	6849	78	301	1.064	2.877	2	I56
455	1.0333	317.5	0.7	3562	20	20	1.235	1.608	2	RST2292BC

Table 1
(Continued)

TOI	Separation (arcsec)	P.A. (deg)	Contrast (<i>I</i> band)	T_{eff} (K)	Distance (pc)	Proj. Sep. (au)	Radius Correction Factor		Prev. Det.?	WDS DD
							(Primary Host)	(Secondary Host)		
1	2	3	4	5	6	7	8	9	10	11
462	0.167	196.1	0.3	5205	205	34	1.326	1.497	1	
463	0.8084	215.0	3.5	6497	177	143	1.02	4.761	1	
476	0.6568	145.4	4.6	7691	226	148	1.007	8.153	1	
487	0.5111	201.0	1.2	5450	125	63	1.154	1.932	2	B2084AB
487	2.993	130.2	5.1	5450	125	374	1.005	10.138	1	
494	2.2257	153.7	5.7	4985	100	222	1.003	13.599	1	
498	2.1845	251.5	3.5	6218	176	384	1.02	4.914	3	RST4412AB
522	0.753	241.1	4.9	7381	109	82	1.005	9.342	1	
527	0.2211	255.9	2.1	7403	163	36	1.07	2.738	1	
550	0.6009	116.1	1.7	5076	62	37	1.1	2.269	1	
563	0.3841	33.4	0.8	5383	157	60	1.216	1.694	1	
568	0.2946	190.7	0.8		305	89	1.216		2	HDS1310
570	2.1638	110.6	6.6	5973	176	380	1.001	19.856	1	
575	0.6293	13.9	4.7	6529	173	108	1.007	8.367	1	
579	0.3303	202.6	3.3	4867	456	150	1.024		1	
593	0.5794	169.7	3.9	7034	411	238	1.014	5.597	1	
594	2.8688	45.3	0.4		308	883	1.301		3	B1595
598	1.7109	290.5	6.2	8324	581	994	1.002	16.803	1	
601	0.1512	352.5	3.1	6106	255	38	1.028	4.219	1	
602	0.976	164.4	3.7	7649	615	600	1.016	5.436	1	
605	0.6548	315.5	1.1	8265	508	332	1.168	1.938	2	JSP296
608	0.248	44.4	0.1	8323	500	124	1.383	1.397	2	RST2587
609	0.3001	91.1	4.0	6272	154	46	1.012	6.107	1	
611	2.3787	93.3	5.5	5689	96	228	1.003	12.33	3	
612	2.0252	98.7	3.9	6422	284	575	1.014	5.69	1	
612	0.1728	145.2	1.5	6422	284	49	1.119	2.079	1	
619	0.2797	234.6	1.0	5096	806	225	1.182		1	
621	2.0655	19.2	6.5	7850	186	384	1.001	19.256	1	
630	0.2099	315.8	3.6	6849	295	61	1.018	5.245	1	
635	1.7656	260.4	4.8	5914	58	102	1.006	9.176	1	
637	2.3926	332.9	5.1	5637	63	150	1.005	10.059	3	
640	0.2498	85.2	4.8	6587	341	85	1.006	8.756	1	
642	0.9513	238.0	2.6		422	401	1.045		1	
644	1.758	132.4	0.4	6112	1330	2338	1.301		2	RST2447
645	4.0745	109.0	1.9	5415	391	1593	1.083	2.505	3	
649	2.6777	130.3	3.2		430	1151	1.026		1	
651	3.608	191.7	2.2		86	310	1.064		3	BU17AB
658	3.88	67.2	0.7	6521	245	950	1.235	1.627	3	HJ4275
659	3.8774	67.2	1.0	5990	201	779	1.182	1.779	3	
666	0.248	257.4	2.8	6680	149	36	1.037	3.601	1	
676	1.5023	260.6	1.5	5430	545	818	1.119	2.151	3	
680	0.7809	331.0	4.3	5967	158	123	1.009	6.942	1	
684	0.2974	303.3	3.1	9488	580	172	1.028	4.103	1	
690	0.2221	292.4	1.2	5538	144	31	1.154	2.026	1	
697	1.1597	138.2	4.9	5447	92	106	1.005	9.255	1	
697	0.0709	165.9	0.2	5447	92	6	1.353	1.43	1	
703	1.4153	221.8	4.7	5384	111	157	1.007	8.449	1	
758	0.1738	349.0	1.1	6072	154	26	1.168	1.907	1	
759	2.694	234.6	3.6	6107	660	1778	1.018	5.257	3	
772	2.3419	165.3	5.8	5184	130	304	1.002	14.246	3	
779	1.5378	165.3	4.8		273	419	1.006		1	
831	0.167	327.9	1.4	5808	86	14	1.129	1.941	2	RST1830
832	3.2133	63.9	4.7	5623	278	893	1.007	8.384	1	
837	2.3128	281.7	4.6	6513	136	314	1.007	7.995	3	
847	1.2446	317.1	0.7	6055	659	820	1.235		3	
851	1.8583	253.8	5.2	5782	155	288	1.004		3	
905	2.2757	100.8	5.9	5565	153	348	1.002	15.332	3	
906	1.246	50.8	2.8	5954	138	171	1.037	3.575	2	RST805
907	3.6665	52.0	1.1	6272	307	1125	1.168	1.852	3	
914	0.104	171.3	0.1	5321	233	24	1.383	1.35	1	
926	0.1903	159.6	2.2	5621	216	41	1.064	2.802	1	
930	0.692	32.6	2.5	6380	99	68	1.049		2	B1455

Table 1
(Continued)

TOI	Separation (arcsec)	P.A. (deg)	Contrast (I band)	T_{eff} (K)	Distance (pc)	Proj. Sep. (au)	Radius Correction Factor		Prev. Det.?	WDS DD
							(Primary Host)	(Secondary Host)		
1	2	3	4	5	6	7	8	9	10	11
931	0.1118	56.8	0.3	6434	691	77	1.326		1	
952	1.1682	135.0	4.7	7025	461	538	1.007	8.607	1	
952	0.1176	59.4	3.6	7025	461	54	1.018	5.245	1	
954	2.3471	50.2	6.2	5820	232	544	1.002	15.699	1	
1033	0.2684	220.4	1.7	6113	219	58	1.1	2.367	1	
1049	1.2782	154.2	5.6	6599	389	497	1.003	12.617	1	

Note. Columns (1)–(4) give the properties of companions to TOIs detected by SOAR. Uncertainties for these measurements and the observation epoch are provided in Table 6 in the Appendix. Columns (5) and (6) give the effective temperature and distance to the TOI given in the TIC (Stassun et al. 2019). Column (7) gives the projected separation of the companion (assuming it is physically associated with the primary) derived from the on-sky separation measured by SOAR and the distance to the star. Columns (8) and (9) give the radius correction factor for hosted planets in each system due to the contamination from the detected star in the scenarios in which the primary is the planetary host and the physically associated secondary is the planetary host. Column (10) is a flag denoting a previous detection of each companion. The flags are (1) new pair, contamination not included in the TIC; (2) known pair, contamination not included in the TIC; and (3) known pair, contamination included in the TIC. Column (11) provides the discoverer designation code if the companion is in the Washington Double Star Catalog maintained by the USNO. Explanations for codes are available at <https://www.usno.navy.mil/USNO/astrometry/optical-IR-prod/wds/WDS>.

3.3. Close Binary Inference with Gaia DR2

While *Gaia* DR2 typically cannot resolve binaries with separations less than approximately $0''.7$ (Ziegler et al. 2018a), the additional source does often result in spurious astrometric solutions. The reliability of the *Gaia* astrometry is quantified by the renormalized unit weight error (RUWE),¹² which is near 1.0 for single sources, with a greater value (for instance, >1.4) indicating a nonsingle or otherwise extended source. Sources with only a two-parameter astrometric solution have null RUWE values.

We find that for the 135 observed *TESS* planet candidate hosts observed with SOAR with RUWE values >1.4 , 114 had resolved companions. Twelve of the observed targets had null RUWE values, and all 12 had bright, close companions ($\Delta\text{mag} < 2$ and $0''.1 < \rho < 0''.5$). For the observed targets with either high or null RUWE values, approximately 86% had companions, typically within the *Gaia* DR2 binary resolution limit of $0''.7$. The median RUWE value for resolved close binaries ($\rho < 0''.75$) is 5.56, compared to 1.04 for wider binaries ($\rho > 0''.75$) and 1.03 for single targets. Only six targets with close binaries have RUWE values less than 1.4, five (TOIs 264, 476, 575, 609, and 640) of which have high contrasts ($\Delta\text{mag} > 4$) and one (TOI-379) of which has a very low separation ($\rho = 0''.03$). The RUWE values and properties of resolved systems are plotted in Figure 4.

It is unclear why some single stars (21 out of 412 observed) have high RUWE values. One possibility is the number of *Gaia* observations of each star. *Gaia* uses a scanning law that passes through the north and south ecliptic poles every 6 hr, resulting in approximately twice as many observations at mid-ecliptic latitudes as near the ecliptic plane or poles (Gaia Collaboration et al. 2016). A Kolmogorov–Smirnov test, however, finds the distribution of ecliptic latitudes for single stars with high and low RUWE values to be similar. The distribution of *Gaia* magnitudes and nearby stellar densities (determined in Section 2.4) of single stars with high and low RUWE values was also similar.

¹² Described in detail in the *Gaia* DPAC public documentation, available at https://gea.esac.esa.int/archive/documentation/GDR2/Gaia_archive/chap_datamodel/sec_dm_main_tables/ssec_dm_ruwe.html.

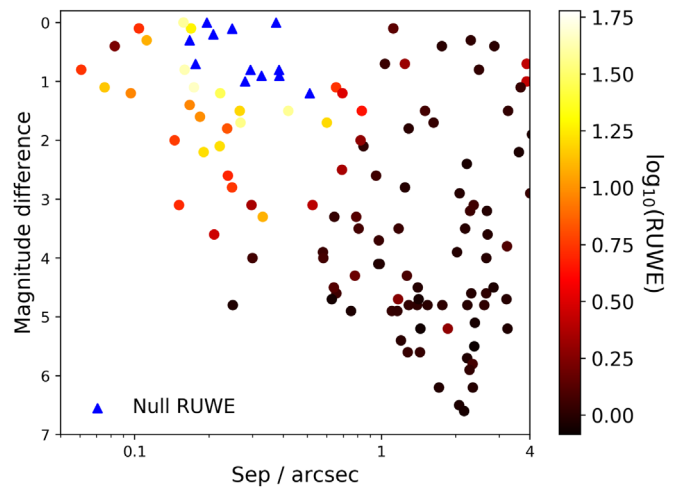


Figure 4. Properties of companions to *TESS* planet candidate hosts resolved by SOAR, colored by the logarithm of each system’s *Gaia* DR2 RUWE value, a metric quantifying the quality of the *Gaia* astrometric solution. Companions in systems with null RUWE values are indicated by blue triangles. While *Gaia* does not resolve close binaries ($\rho < 0''.7$), the high or null RUWE value may be used to infer the existence of a companion star. This method is successful with an accuracy of 86% in our survey.

It is also possible that the anomalously high RUWE values for single stars are a result of binaries not detected by the SOAR speckle observations, such as those with close separations or high magnitude differences outside the sensitivity of SOAR. Further observations with larger-aperture telescopes and laser guide star AO could confirm whether these single stars have companions. Of the 21 single stars with high RUWE values, five have the results of additional high-resolution imaging available on ExoFOP.¹³ None of the five targets had a detected companion star.

¹³ TOI 271 was observed with NaCo on the VLT (posted by Elisabeth Matthews), TOI 502 was observed with NIRC2 on Gemini-North (Elisabeth Matthews) and NIRC2 on Keck II (David Ciardi), TOI 674 was observed by NIRC2 on Gemini-North (Ilan Crossfield/Elisabeth Matthews), and TOI 254 and 311 were observed by PHARO on the Palomar 5 m (David Ciardi).

Checking for a high or null RUWE value can serve as an excellent first check for potential companion stars in *TESS* systems, although further high-resolution observations would still be required to determine the properties of a purported companion. The clustering of binary systems with null RUWE values in a region of similar separation and magnitude difference, however, could even be used to infer the vague properties of a subset of the unresolved stars in *Gaia* DR2.

4. Impact of Binary Stars on the *TESS* Planetary Systems

The presence of a binary companion can result in a dynamically harsh environment, reducing the probability that a planetary system can form and survive. Some planets are found in close binary systems, however. In this section, we search for further insight into the impact binary stars have on the *TESS* planet population.

4.1. Preparation of the Sample

To facilitate an analysis of the multiplicity of our observed targets, some sample preparation was required.

The speckle imaging is a snapshot of the host systems, providing an on-sky angular separation between the primary and secondary star. To determine the projected physical separations, the distance to each system is required. We collect distances to each of these targets from *Gaia* DR2 (Bailer-Jones et al. 2018), when available. However, *Gaia* can provide spurious astrometric solutions in the case of close, unresolved binaries (Arenou et al. 2018). So, when the *Gaia* distance errors are large (greater than 20%), we use the distances reported in the TIC (Stassun et al. 2019), which were derived using inverse Stefan–Boltzmann relations based on V magnitudes. The distances used for each target in this analysis are available in Table 1.

We prepare our sample by removing stars with T_{eff} in the TIC inconsistent with an FGK-type star (i.e., $T_{\text{eff}} > 7200$ and < 3900 K) using the relations of Pecaution et al. (2012). We also remove binaries with contrasts indicating mass ratios $q < 0.4$. These systems, with high magnitude differences, are significantly more likely to be chance alignments based on the analysis in Section 2.4, and their exclusion enables comparisons between the *Kepler* (Kraus et al. 2016) and *TESS* sample. We determine q by finding the mass of the primary star based on its likely spectral type estimated using the T_{eff} reported in the TIC and the secondary star based on the magnitude difference with the primary (Kraus & Hillenbrand 2007). We also remove systems with a *TESS* follow-up disposition of false positive and only a single transit detected by *TESS*. After these cuts, our sample includes 455 stars observed with SOAR.

To improve our coverage of wide binaries, we include companions to these 455 SOAR targets found in *Gaia* DR2 (Gaia Collaboration et al. 2018) with proper motions and distance estimates (Bailer-Jones et al. 2018) consistent at 2σ . We search out to an on-sky angular radius equivalent to a 5000 au projected separation based on the *Gaia* distance estimate. El-Badry & Rix (2018) found that the proper motion of wide binaries can vary significantly because of orbital motion. For each star, we calculate the maximum Keplerian orbital on-sky motion as a function of projected separation. The proper motion of each nearby *Gaia* star is allowed to vary by this orbital motion in our binary detection. The *Gaia* DR2 binaries used are listed in Table 5 in the Appendix. Only pairs

of stars with contrasts consistent with mass ratios $q > 0.4$ were included. Ziegler et al. (2018a) provided the binary recovery sensitivity of *Gaia* DR2.

4.2. Multiplicity of Solar-type *TESS* Planet Candidate Hosts

Close binaries can provide many potential obstacles to planet formation and evolution. In a large survey of *Kepler* planets, Kraus et al. (2016) found that far fewer planets were detected around stars with companions at solar system scales within approximately 50 au. The *TESS* sample is quite disparate in several ways from the *Kepler* sample, as shown in Figure 1. In general, the *TESS* planets are somewhat larger and at shorter periods than the *Kepler* planets, a consequence of the *TESS* photometric precision and survey strategy. Unlike *Kepler*, the *TESS* planets are spread across the sky and sample a more diverse set of the Galactic stellar population, providing an opportunity to confirm and characterize the effect of binaries.

To understand how binaries impact planetary systems, we compare our sample to a simulated survey of field solar-type stars. We use the field binary statistics of Raghavan et al. (2010), who found a flat eccentricity distribution, a lognormal period distribution (with a mean of $\log P = 5.03$, corresponding to an orbital semimajor axis of approximately 50 au, and $\sigma_{\log P} = 2.28$), and a nearly uniform mass ratio distribution (with a sharp increase near-equal-mass ratio) in the population of solar-type field binaries. We follow the procedures of Kraus et al. (2016) to account for projection effects, Malmquist bias, and the detection limits of our survey. We also account for the reduced sensitivity of *TESS* to planet transits due to dilution by the stellar companion.

For each solar-type star observed in our survey, a Monte Carlo model was constructed to determine the expected number of binary companions at a range of projected separations between 1 and 5000 au. In each of 10^5 iterations, there was a $33\% \pm 2\%$, $8\% \pm 1\%$, and $3\% \pm 1\%$ probability that one, two, or three companion stars would be populated, respectively (the observed multiplicity of solar-type stars). Since binaries are overrepresented in flux-limited surveys (Schmidt 1968), we correct for Malmquist bias by adjusting this probability by an additional factor equal to the fractional volume excess in binaries due to their relative brightness, $V_{\text{bin}}/V_{\text{single}}$. The period, eccentricity, and mass ratio of these binaries were drawn from the distributions reported in Raghavan et al. (2010). The period was converted to a semimajor axis using the TIC estimated stellar masses. We select uniformly distributed values for the cosine of inclination, the position angle of the ascending node, the longitude of periastron, and the time of periastron passage. Finally, the instantaneous separation was projected to the distance to the primary star as reported in *Gaia* DR2. The mass ratio was converted to an approximate magnitude contrast using the relations in Kraus & Hillenbrand (2007), and possible detection by SOAR speckle imaging and *Gaia* DR2 was determined using the measured sensitivity limits and the companion’s contrast and separation. We use the ratio of nondetected binaries to the total number of binaries at each separation to determine a completeness correction due to limitations in the ability to resolve close or wide companions.

The resulting observed binaries of *TESS* planet candidate hosts from SOAR and *Gaia* compared to the expected number derived for field stars are shown in Figure 5. The uncertainty in the expected number of observed binaries at each separation range is derived from the spread of binaries in the simulated

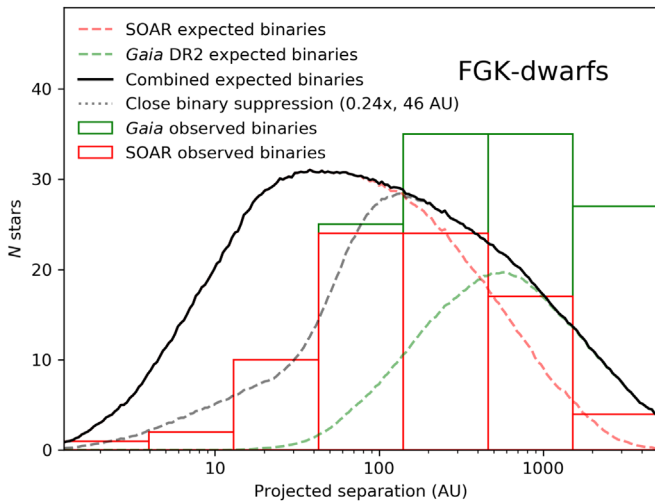


Figure 5. In red and green are the number of observed companions from SOAR and *Gaia* DR2 for solar-type *TESS* planet candidate hosts in logarithmic bins of projected separation of 0.5 dex width. Companions found in both SOAR and *Gaia* are included in the SOAR sample. In black is the expected distribution from a multiplicity study of field stars (Raghavan et al. 2010), combining both field binaries that would be detected by SOAR and *Gaia*. The expected binaries from SOAR and *Gaia* are also plotted individually. These distributions take into account the detection sensitivity of both SOAR and *Gaia*. The observed distribution shows a clear paucity of *TESS* planet candidate host binaries at small projected separations compared to the field stars and the inverse at wide separations. A best-fit model for the close binary suppression applied to the expected distribution of binaries for field stars is also plotted. The best-fit model has binaries suppressed by a factor of 0.24 at physical separations less than 46 au.

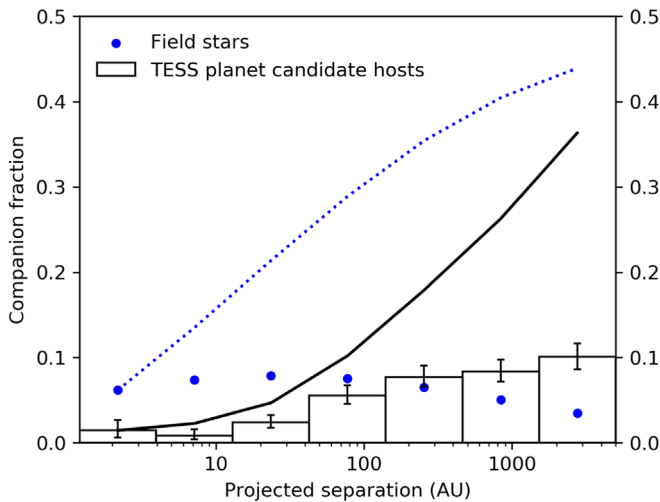


Figure 6. The observed companion rates for the solar-type *TESS* planet candidate hosts, corrected for survey completeness, for logarithmic bins with a width of 0.5 dex are shown by the black bars. The completeness factors are based on the binary statistics of Raghavan et al. (2010) and our detection limits. The estimated companion rates for field stars, plotted by blue points, are included for comparison. The cumulative distributions for the *TESS* planet candidates and field stars are plotted as dotted and solid lines, respectively.

surveys, which propagates the field binary rate uncertainties reported by Raghavan et al. (2010). The observed companion rate to the *TESS* planet candidates as a function of projected separation was determined by dividing the number of observed binaries by the total number of stars observed. The companion rate in each separation bin was then corrected for survey completeness using our measured sensitivity limits. The

companion rates for the *TESS* planet candidate hosts and field solar-type stars are shown in Figure 6. The distributions differ substantially, both at close and wide separations, which we will address in turn.

4.2.1. Bias against Planet Detection in Binaries

The additional flux from a companion star reduces the depth of the transit, making planet detection more difficult, and the TIC (Stassun et al. 2019) was constructed without consideration for potential stellar multiplicity. Left uncorrected, this observational bias would result in fewer binaries being detected among planet hosts, as transiting planets are easier to detect around single stars with no flux dilution.

We quantify the magnitude of this bias using the methods of Wang et al. (2015), adapted for the *TESS* sample. The planet search pipeline for *TESS*, run by the Science Processing Operations Center (SPOC; Jenkins et al. 2016), flags a potential transit candidate if the signal-to-noise ratio (S/N) is greater than 7.1. The S/N can be calculated by the equation

$$S/N = \frac{\delta}{\text{CDPP}_{\text{eff}}} \sqrt{N_{\text{transits}}}, \quad (3)$$

where δ is the transit depth, CDPP_{eff} is the effective combined differential photometric precision per transit, and N_{transits} is the number of observed transits. In the presence of a companion star, the transit depth is reduced due to the additional flux by a factor X given in Equations (1) and (2), depending on the identity of the host star, which likewise reduces the S/N of the detection.

We estimate the detection bias using a simulation for each of the *TESS* systems observed with no binary companion. For every single system, we choose the planet that has the highest S/N and add a companion star, whose mass is drawn randomly from the binary mass distribution described in Raghavan et al. (2010; e.g., uniform with a spike near unity). The transit depth of the planet is calculated for one of two randomly selected scenarios: (1) the planet orbits the primary star with reduced transit depth from the second star, or (2) the planet orbits the secondary with updated transit depth due to the different stellar radius and dilution from the primary star. For the selected scenario, the S/N of the detection is calculated using the new transit depth, and, if greater than 7.1, it was determined that the planet could still be detected by *TESS* with the companion star. This procedure is repeated 10^5 times for each observed *TESS* system to determine α , the probability of a planet detection in that system if a stellar companion is present. The distribution of α for the observed systems is an indication of the magnitude of the binary detection bias (i.e., if most of the observed planets in single systems would still be detectable even with a binary companion, then it is likely that a few additional planet signals were not detected by *TESS* due to dilution from a second star). Relevant data and α -values for each system are provided in the Appendix in Table 3.

We find that most of the *TESS* systems would still be detectable even with an equal-mass companion, with median and mean α -values of 1.0 and 0.97. Significantly more *TESS* planets are detectable with companions compared to the *Kepler* sample of Wang et al. (2015), who found a median value of $\alpha = 0.89$. This is likely due to the larger radii and lower periods of the *TESS* planets, which result in higher S/N. We would expect that 9 ± 2 of the 416 observed single systems

($2.1\% \pm 0.4\%$) would not have planets detected by *TESS* if each were in stellar binaries. Therefore, the number of potential *TESS* planets that were not detected due to binary dilution is likely to be small relative to the number of systems observed, and we expect that the detection bias against planets in binary systems does not significantly impact the subsequent analysis.

In the simulations, the stellar radii are from the TIC. The stellar radii of secondary stars were determined using the mass–radius relationship of Feiden & Chaboyer (2012). The CDPP_{eff} was estimated from the *TESS*-band magnitude of the primary and the photometric precision model of Stassun et al. (2018), interpolated based on the transit duration.

4.2.2. Suppression of Planet-hosting Close Binaries

We find significantly fewer binaries in the *TESS* sample with projected separations of less than 100 au than would be expected for a similar survey of field stars (44 observed binaries compared to an expectation of 124 ± 8 ,¹⁴ a 9.0σ discrepancy). We find a completeness-corrected companion rate for *TESS* planet hosts of $9.8^{+1.5}_{-1.3}\%$ at projected separations of less than 100 au and larger than 1 au. For comparison, we estimate for field stars a companion rate at similar projected separations of $27.7^{+2.0}_{-2.2}\%$ using the binary statistics of Raghavan et al. (2010). *TESS* planet hosts are therefore approximately $3\times$ less likely to have a close binary companion compared to field stars.

Similar to Kraus et al. (2016), the dearth of close binaries for planet hosts can be modeled by a simple two-parameter model using a suppression factor, S_{bin} , that cuts on at some semimajor axis value, a_{cut} . We performed a Markov Chain Monte Carlo (MCMC) analysis to explore 10^6 possible values for S_{bin} and a_{cut} , seeking to reduce the χ^2 goodness of fit to the observed distribution. The resulting distributions are shown in Figure 7. We find the optimal values for the suppression with 68% credibility ranges to be $S_{\text{bin}} = 24^{+11}_{-7}\%$ and $a_{\text{cut}} = 46^{+22}_{-15}$ au, shown in Figure 5. These values are in agreement with those found by Kraus et al. (2016) for *Kepler* planet candidates ($S_{\text{bin}} = 34^{+15}_{-14}\%$ and $a_{\text{cut}} = 47^{+59}_{-23}$ au), and again, the null hypothesis (i.e., the field and planet candidate host distribution are similar with no binary suppression occurring) is strongly disfavored at 9.8σ .

4.2.3. Enhancement of Wide Binaries in Systems with Large Planets

At wide separations, more binaries were detected around the *TESS* planet candidate hosts compared to the field stars: 119 observed binaries with projected separations greater than 100 au, compared to an expected number of 77 ± 7 , a 4.9σ discrepancy.

The wide binaries being detected are almost exclusively those hosting the large planet candidates. This is readily apparent if we split our sample into two bins using a radius cut of $9 R_{\oplus}$ (approximately the size of Saturn), as shown in Figure 8. We find that both populations of 244 small and 199 large planets exhibit a paucity of systems in close binaries. At wide separations, however, the companion rates for the two populations diverge: at projected separations greater than 200 and 10^3 au, large planet hosts have completeness-corrected companion rates of $47.8\% \pm 3.8\%$ and $30.4\% \pm 3.4\%$, respectively. For small planet hosts, the companion rates for

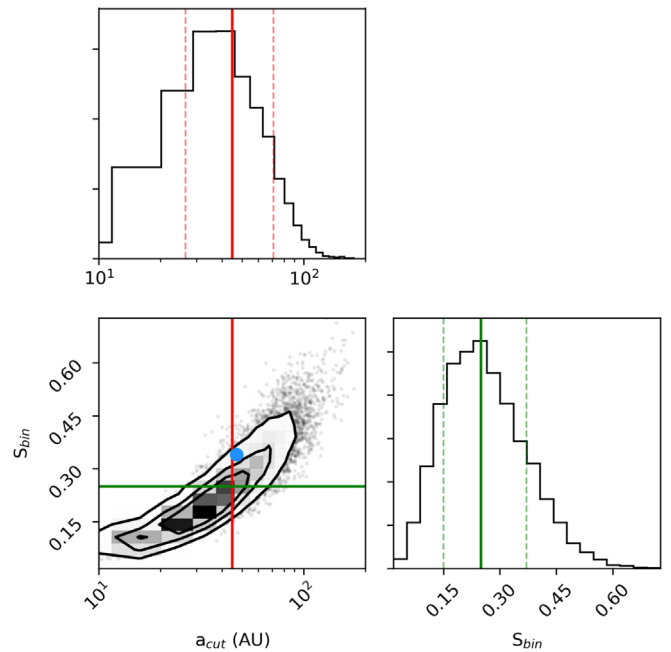


Figure 7. Distributions of suppression factors and semimajor axis cuts from 10^6 chains of an MCMC analysis to model the observed close binary suppression seen in systems with *TESS* planet candidates. Solid lines indicate the median value of each distribution ($a_{\text{cut}} = 46$ au and $S_{\text{bin}} = 0.24$), and dashed lines mark the 68% confidence interval. The two parameters are correlated, such that less suppression is required if the semimajor axis cutoff is larger, and vice versa. A blue circle marks the values of the best-fit model from the *Kepler* sample of Kraus et al. (2016).

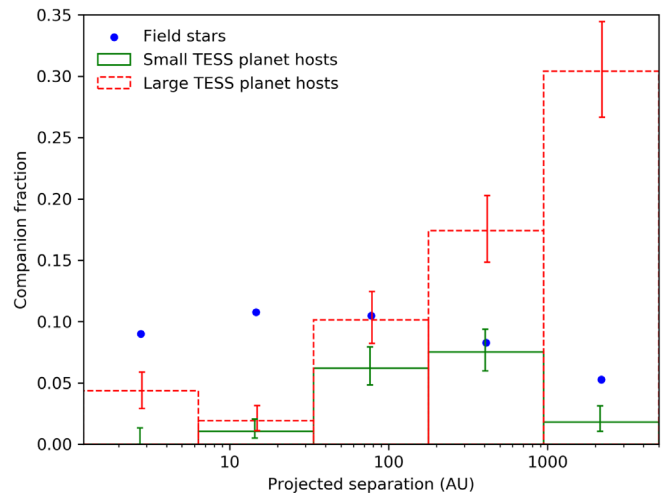


Figure 8. Completeness-corrected companion fraction per 0.5 dex bins in projected separation for small and large *TESS* planet candidate hosts observed in this survey. For reference, the separation distribution of field binaries from Raghavan et al. (2010) is included. Both populations of *TESS* planet hosts have suppressed rates of close binaries but diverging binary rates at wide projected separations. Large planets ($R_p > 9 R_{\oplus}$) are approximately $3.5\times$ more likely to be found in a wide binary, compared to field stars. Conversely, small planets are $2\times$ less likely to be found in a wide binary.

similar projected separation ranges are $6.4^{+1.5}_{-1.1}\%$ and $1.8^{+1.3}_{-0.7}\%$, respectively. Thus, the two populations have discrepant companion rates for projected separations greater than 200 and 10^3 au with significances of 9.8σ and 8.1σ , respectively.

The companion rates for the small and large planets at wide separations are also both significantly divergent from that of

¹⁴ Uncertainties in the expected number of observed binaries are derived from the resulting distribution of simulated surveys, as described in Section 4.2.

field stars. We estimate from the distribution of Raghavan et al. (2010) that field stars have a companion rate of 13.7% and 5.3% at projected separations greater than 200 and 10^3 au, respectively. Therefore, large *TESS* planets are approximately a factor of 3.5 more likely to be hosted in a wide binary than would be expected. Conversely, small *TESS* planets are $2\times$ less likely to be found in a wide binary system than would be expected from field star statistics.

4.3. Binary Fraction of M Dwarf Planet Candidate Hosts

We observed 44 planet candidate hosts with T_{eff} estimates in the TIC consistent with an M dwarf ($T_{\text{eff}} < 3900$ K; Pecaut et al. 2012). We detected companions to 16 of these hosts, for a multiplicity fraction of $36\% \pm 9\%$. This is consistent with the field star M dwarf multiplicity fraction of $26.8\% \pm 1.4\%$ found by Winters et al. (2019).

To compare the separation distribution of planet candidate M dwarf hosts to the field star population, we use the companion fraction, the lognormal projected separation distribution (peaking at 20 au with $\sigma_{\log a} = 1.16$), and the uniform mass ratio distribution (with a slight increase in near-equal-mass binaries) found by Winters et al. (2019). The resulting distribution is shown in Figure 9.

We find fewer close binaries than would be expected for the M dwarf planet candidate hosts: two observed compared to approximately 11 expected at projected separations of less than 100 au. We also find a large number of companions at wider separations: 14 observed companions at projected separations between 100 and 5000 au, compared to approximately five that would be expected.

Both of these results mirror those found with the solar-type sample. We do not see a large number of companions at very wide projected separations ($s > 1000$ au). This may, in part, be due to the M dwarf projected separation distribution peaking at lower separations (~ 20 au rather than ~ 50 au) and with lower variance than the solar-type sample. Also, as shown in Section 4.2.3, the widest binaries typically host Jupiter-sized planets, which are inherently rare around M dwarfs (Dressing & Charbonneau 2013).

4.4. Mass Ratios of Planet Candidate Host Binaries

The mass ratio, or q , distribution of solar-type binary systems was found to be nearly uniform by Raghavan et al. (2010), with an increase for near-equal-mass binaries. Winters et al. (2019) found a similar distribution at high- q for M dwarfs. Ngo et al. (2016) found that the mass ratio distribution for hosts of hot Jupiters was heavily weighted toward low- q companions.

The mass ratio distribution of resolved *TESS* planet candidate hosts may vary significantly from that of field stars. To compare the two populations, we use the mass ratios derived from the observed magnitude difference, as described in Section 4.1, for the SOAR binaries, while for the field stars, we use the mass ratios from the simulation described in Section 4.2, which takes into account our survey sensitivity.

The observed and expected mass ratio distribution of binaries to *TESS* planet candidate hosts is shown in Figure 10. The mass ratio distribution of observed binaries is consistent with being uniform for $q > 0.4$; for lower mass ratios, the SOAR sensitivity is low. There is no significant difference in the distribution for small and large planets (cut at

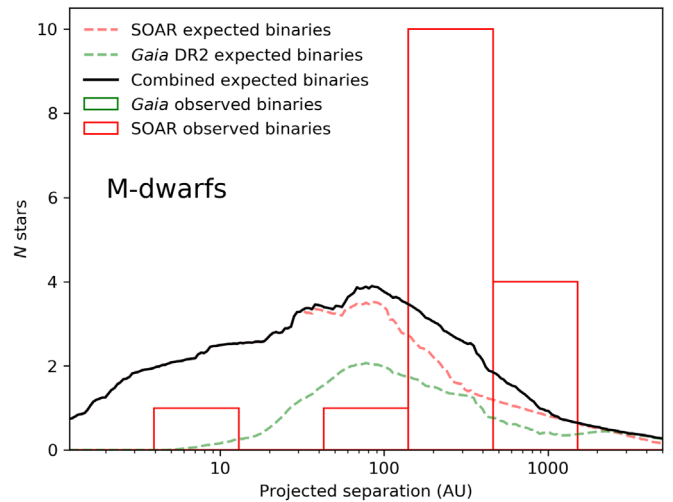


Figure 9. Similar to Figure 5 for *TESS* M dwarf planet candidate hosts, using the field binary statistics of Winters et al. (2019). As with the solar-type stars, the M dwarf planet candidate hosts have a deficit of close binaries at separations less than 100 au and a surplus of wide binaries separated by more than 100 au.

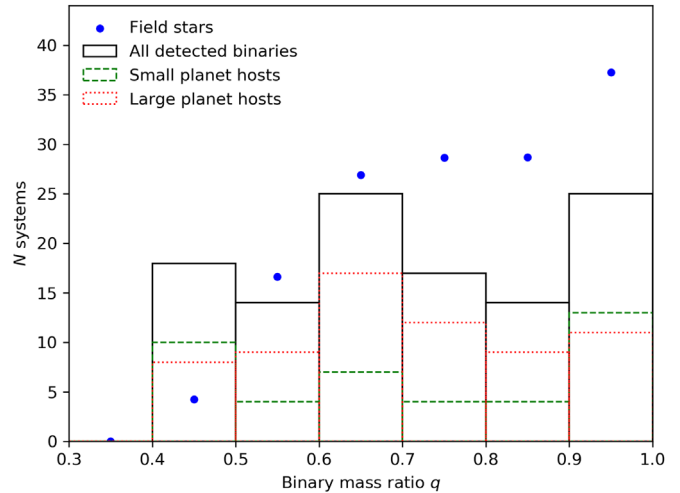


Figure 10. Mass ratio distribution of all observed binaries to *TESS* planet candidates resolved in SOAR speckle imaging, including the individual distributions for large and small planet candidate hosting stars. The expected distribution of observed binaries based on the near-uniform mass ratio distribution of field stars (Raghavan et al. 2010) and the survey sensitivity is included. The observed mass distribution is consistent with uniform.

$9 R_{\oplus}$). Compared to the expected number based on field star statistics, we find slightly fewer high- q binaries, due in part to binary suppression at low separations, and slightly more low- q binaries, which is likely to be, at least in part, a consequence of unassociated field star contamination as the companions with large magnitude differences are at wide separations.

5. Binary Impact on the Galactic Planet Population

Approximately half of the solar-type field stars in our galaxy are found with a stellar companion, and, as discussed in Section 1, the impact binaries have on the planet population is potentially large. The *TESS* sample is not statistically complete, containing a combination of small planets, similar to the majority of planets detected by *Kepler*, and many large planets,

similar to the extensively studied population of hot Jupiters (e.g., Wu et al. 2007; Knutson et al. 2014; Evans et al. 2016; Ngo et al. 2016). In our data, we see a combination of two separate effects found individually in previous studies: suppression of planets in binaries at low separations and enhancement of binaries at wide separations.

Follow-up observations of the planet candidate hosts found in the *Kepler* survey gave some insight into how binaries impact planetary systems. Wang et al. (2015) found some evidence in radial velocity trends that binaries at separations < 100 au may suppress planet occurrence. Kraus et al. (2016) found that approximately a fifth of the solar-type stars are not able to host planets due to the influence of stellar companions. Significant suppression in the rate of spectroscopic binaries hosting planets was detected by Ngo et al. (2016), which helps rule out an unresolved population of very close stellar companions. We find similar suppression of close binaries among the *TESS* planet candidates, suggesting that this effect is likely prevalent throughout the Galaxy in regions of varying stellar density and age. The suppression of close binaries is apparent regardless of cuts in the orbital period, planetary radii, or stellar effective temperature.

As noted by Kraus et al. (2016), it is not clear why some close binaries are able to host planets with all of the theoretical obstacles to their formation and survival. Many of the *TESS* binaries that are close in projection likely have short orbital periods, meaning that their motion may be detected over the coming years. Continued monitoring can provide orbital solutions for these systems to find a true physical separation rather than the projected separation presented here. Studying these orbits may provide insight into the conditions that exist such that planets may form and survive in the chaotic regime around close binaries.

It is possible that the enhanced companion fraction for small planets may be, at least in part, due to observation effects: the false-positive rate of giant planets in transiting planet surveys has been found to be larger than that for smaller planets (Fressin et al. 2013). The radii of Jupiter-mass planets and brown dwarfs are similar, and mass constraints are required to confirm each planet. However, brown dwarfs on close transits seem to be inherently rarer than massive planets (Bowler 2016). In addition, while a planet is more likely to be hosted by the primary star in the majority of systems (Gaidos et al. 2016), multiple star systems will have some enhancement in planet occurrence due to having additional potential hosts.

The exclusion of previously confirmed planets from our target list, as discussed in Section 2, may result in a bias in our sample. Many of these confirmed planets were detected in ground-based surveys, which may avoid resolved binaries (Street et al. 2003; Bakos 2018), or avoid following up systems with binary indicators, such as multiple sets of spectral lines (Triaud et al. 2017). In addition, the contamination from unresolved, near-equal-mass binaries may result in the nondetection of planets by ground-based surveys (Bouma et al. 2018). Some of these planets may subsequently be detected by *TESS*. These observational biases could result in an inflated companion rate for the newly detected *TESS* systems in our survey.

Previous binary surveys of large planet hosts that were detected exclusively from ground-based surveys find a similar enhancement in binaries at wide separations. Ngo et al. (2016) found that stars hosting hot Jupiters were approximately three

times more likely to have stellar companions than field stars. Fontanive et al. (2019) found a wide binary fraction (20–10,000 au separations) for gas giants approximately twice that of field stars. Similarly, Ziegler et al. (2018c) found that the large, close-in *Kepler* planets were significantly more likely to have companions than other populations of planets. We find a similar effect for our sample as a whole. However, closer analysis reveals that this enhancement is due only to the systems hosting the largest planets. Indeed, a suppression effect is also seen for small planets in binaries at very wide projected separations ($s > 1000$ au).

There are two possible physical scenarios that could lead to a high companion fraction for systems hosting hot Jupiters: first, the binary companion may encourage in some manner the formation of large planets; and second, large planets form at similar rates in single and multiple star systems, but in binaries, the companion star drives large planets inward to the low-period regime probed by *TESS*. For the former, there is evidence that a stellar companion can lead to density waves in the protoplanetary disks (Dong et al. 2015). These high-density regions can subsequently seed the formation of planetesimals (Carrera et al. 2015). In addition, the protoplanetary disks around binary stars may have more mass than around single stars, which simulations suggest leads to larger planets (Mordasini et al. 2012).

The high number of gas giants in binaries coupled with the low number of observed smaller planets may be explained by planet–planet scattering during migration. In other words, the orbits of the inner smaller planets may be altered by the gas giants being driven inward to low-period orbits. In one possible scenario, Kozai–Lidov instabilities induced by the stellar companion may initially drive the gas giant to a highly eccentric orbit (Holman et al. 1997; Naoz et al. 2011). Ngo et al. (2016) and Fontanive et al. (2019) found that the Kozai–Lidov effect alone was insufficient to explain the observed population of hot Jupiters. In scattering events, large planets on wide orbits are preferred, as quantified by the Safronov number (Ford & Rasio 2008). The highly eccentric gas giant in this scenario would dominate the inner planets as it nears perihelion, resulting in planet scattering events (Fabrycky & Tremaine 2007). Eventually, the gas giant orbit will circularize to a low-period orbit due to planet–star tidal friction (Jackson 2009). Observational evidence suggests that planetary interactions during secular migration are not unusual: around a quarter of hot Jupiters are found on retrograde orbits, only possible through close planetary perturbations (Naoz et al. 2011; Ngo et al. 2015).

Dynamical interactions between planets with high mass disparities may dramatically alter the orbital inclination of the smaller planet, in many cases to a nontransiting orientation (Hamers 2017), or drive the smaller planets to highly eccentric orbits (Xie et al. 2016) and possibly even ejection from the system (Davies et al. 2014). Planet–planet scattering has been shown to largely reproduce the observed distribution of eccentricities in transiting planets (e.g., Ford & Rasio 2008; Jurić & Tremaine 2008; Raymond et al. 2011). Numerical investigations suggest that instabilities in giant planet orbits are likely destructive to inner terrestrial planets (Veras & Armitage 2006; Matsumura et al. 2013). Indeed, *Kepler* found that only a small fraction of small, close-in planets had gas giants in nearby orbits (Lissauer et al. 2011; Ciardi et al. 2013; Huang et al. 2016). Lastly, Wang et al. (2015) found that systems

hosting small planets had fewer companions than field stars at separations up to 1500 au, compared to 100 au for systems with hot Jupiters. As they noted, another possible explanation for this disparity is that the relative timescales of pericenter and nodal precession increase as planetary mass decreases (Takeda et al. 2008). Thus, for small planets, the Kozai timescale will be shorter than precession. Consequently, the weaker planet–planet coupling means smaller planets are more prone to the influence of distant stellar companions.

6. Conclusions

We searched 542 *TESS* planet candidate hosts for companions using SOAR speckle imaging. We found 123 companions within 3'' of 117 targets. Contamination from these companions in the *TESS* light curves results in the radii of planet candidates in these systems increasing by a factor of 1.11, assuming the primary star is indeed the host. We find that *TESS* planet candidate hosts are around $3.5\times$ less likely to have stellar companions at projected separations less than approximately 50 au than field stars. The destructive impact of close binaries, previously seen in the *Kepler* sample, is apparent in the local Galaxy. We also detect far more large planets and far fewer small planets in wide binaries than would be expected for field stars. This may be evidence of chaotic secular migration of gas giants resulting from perturbations from the binary companion inducing planet–planet scattering. The M dwarfs hosting planet candidates have a similar binary pattern as the solar-type sample. The mass ratio distribution of planet candidate hosting stars is consistent with uniform, as is seen in field stars.

Future multiband speckle observations by SOAR of the resolved binary systems hosting *TESS* planets will be able to determine the probability that the companions are indeed physically associated. In addition, multi-epoch observations over the coming years will be able to check for common proper motion and solve the orbits of bound systems, providing the semimajor axis and eccentricity of the binary systems hosting planets. Analysis of these binaries may provide insight into how some close systems were able to form and maintain their planetary populations. Lastly, the detection of northern planet candidates by *TESS*, beginning in 2019, will provide many more nearby planet-hosting systems. Their proximity will allow efficient instruments on moderate-sized telescopes in the north, such as Robo-AO on the University of Hawaii 88 inch (Baranec et al. 2017), to detect companions at solar system scales.

We thank the anonymous referee for a careful analysis and useful comments on the manuscript.

C.Z. is supported by a Dunlap Fellowship at the Dunlap Institute for Astronomy & Astrophysics, funded through an endowment established by the Dunlap family and the University of Toronto. A.W.M. was supported by NASA grant 80NSSC19K0097 to the University of North Carolina at Chapel Hill.

Based on observations obtained at the Southern Astrophysical Research (SOAR) telescope, which is a joint project of the Ministério da Ciência, Tecnologia, Inovações e Comunicações (MCTIC) do Brasil, the U.S. National Optical Astronomy Observatory (NOAO), the University of North Carolina at Chapel Hill (UNC), and Michigan State University (MSU).

This paper includes data collected by the *TESS* mission. Funding for the *TESS* mission is provided by the NASA Explorer Program. This work has made use of data from the European Space Agency (ESA) mission *Gaia* (<https://www.cosmos.esa.int/gaia>), processed by the *Gaia* Data Processing and Analysis Consortium (DPAC; <https://www.cosmos.esa.int/web/gaia/dpac/consortium>). Funding for the DPAC has been provided by national institutions, in particular the institutions participating in the *Gaia* Multilateral Agreement. This research has made use of the Exoplanet Follow-up Observation Program website, which is operated by the California Institute of Technology, under contract with the National Aeronautics and Space Administration under the Exoplanet Exploration Program. This work made use of the Washington Double Star Catalog maintained at USNO.

Facilities: SOAR (HRCam), *TESS*, *Gaia*.

Software: astropy (Astropy Collaboration et al. 2013; Price-Whelan et al. 2018), emcee (Foreman-Mackey et al. 2013), corner (Foreman-Mackey 2016).

Appendix

In Figures 11–14 we show the speckle autocorrelation functions from SOAR speckle observing of *TESS* planet candidate host stars with resolved nearby stars. In Table 2, we detail the crossmatch between SOAR detected binaries and nearby stars in the TIC. In Table 3, we list the estimated bias against detection of planets within multiple star systems by *TESS*. In Table 4, we detail the crossmatch between SOAR detected binaries and nearby stars in *Gaia* DR2. In Table 5, we detail nearby stars in *Gaia* DR2 that were not detected by SOAR. In Table 6, we provide the full SOAR speckle observation list and binary properties.

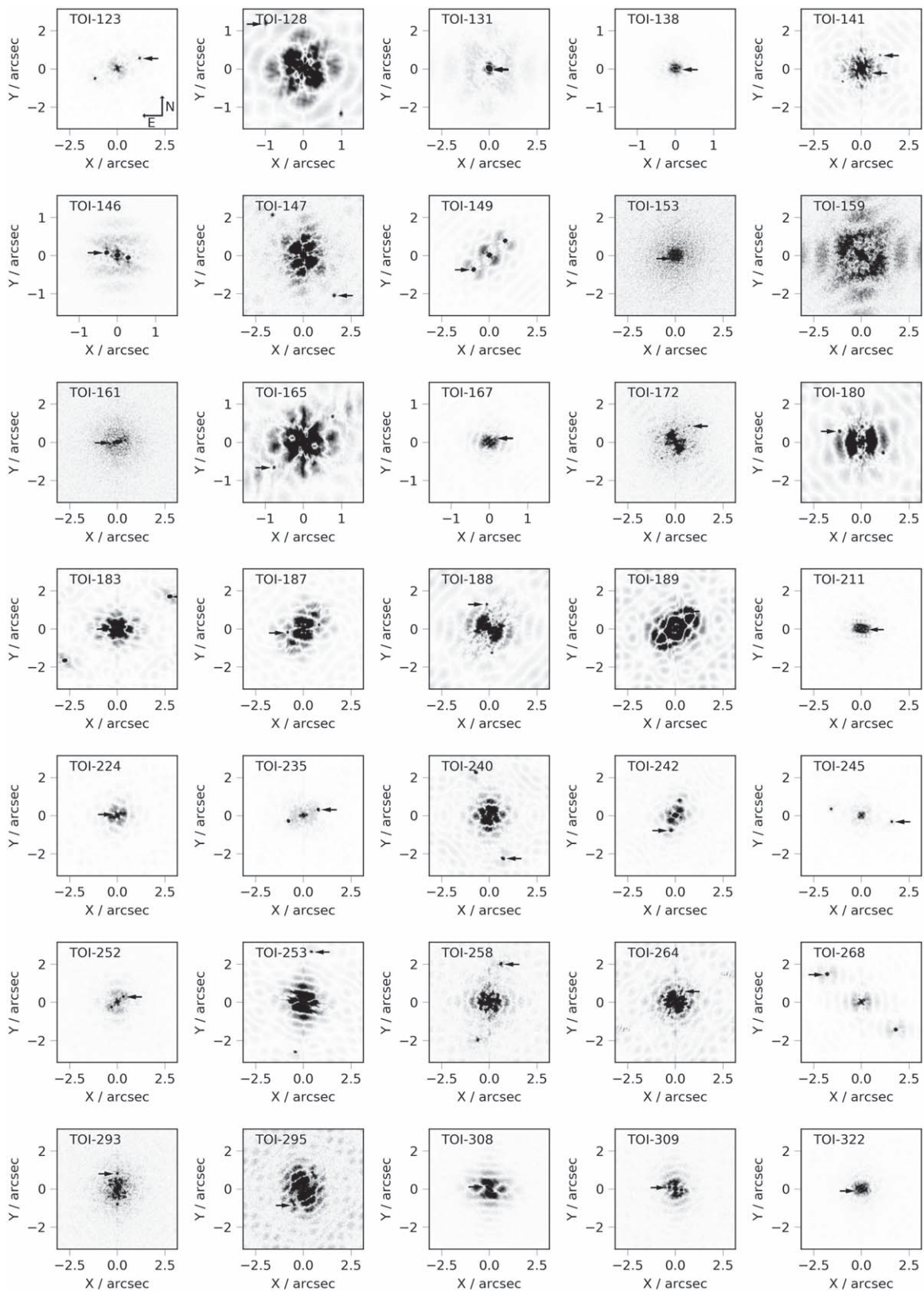


Figure 11. Speckle ACFs from SOAR speckle observing of *TESS* planet candidate host stars with resolved nearby stars. Each nearby star is mirrored in the images, with the true location marked by an arrow. Images are presented with an inverse linear scale for clarity. The orientation is similar in all images, with north pointed up and east to the left. A compass is shown in the top left image for reference.

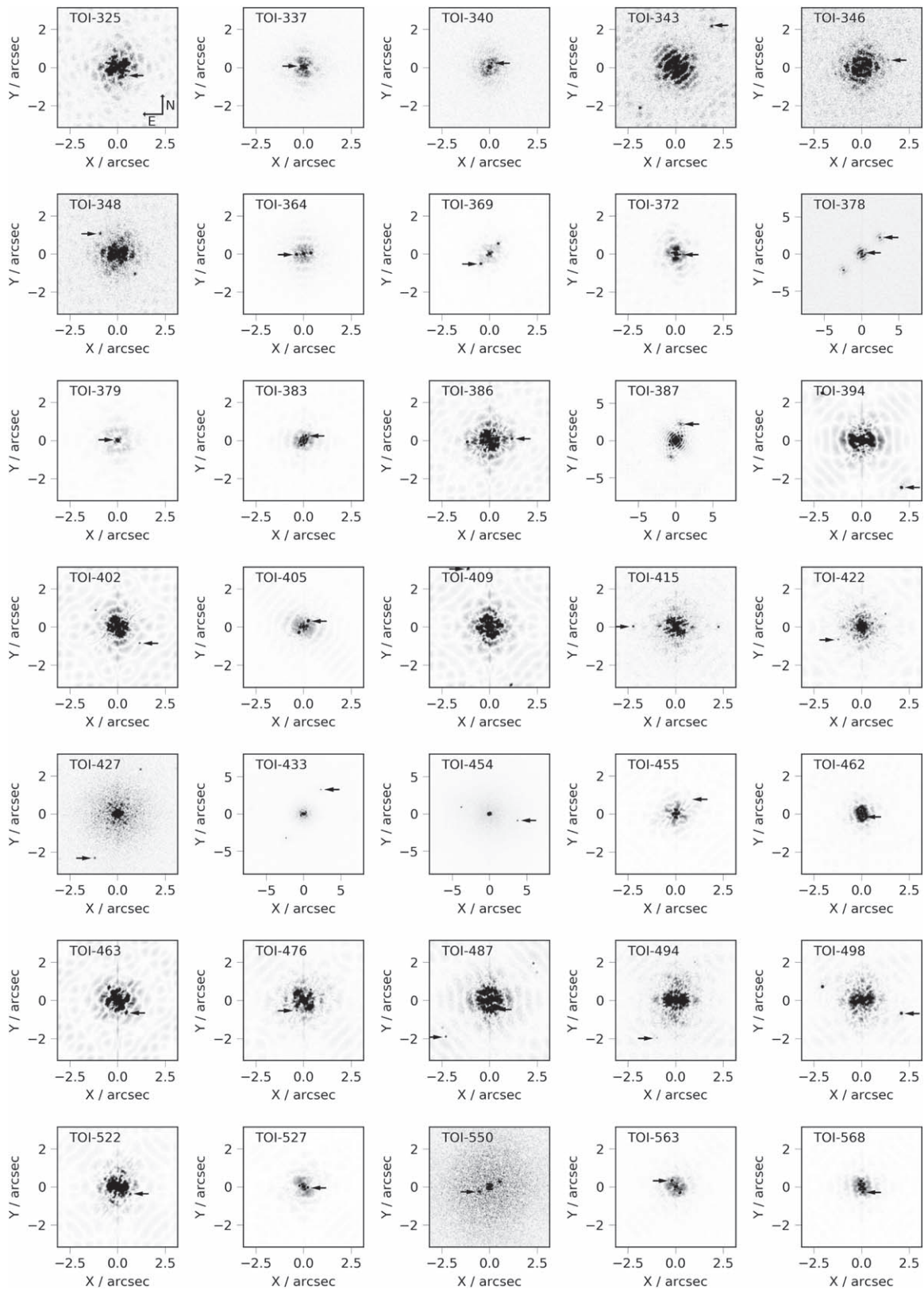


Figure 12. Similar to Figure 11.

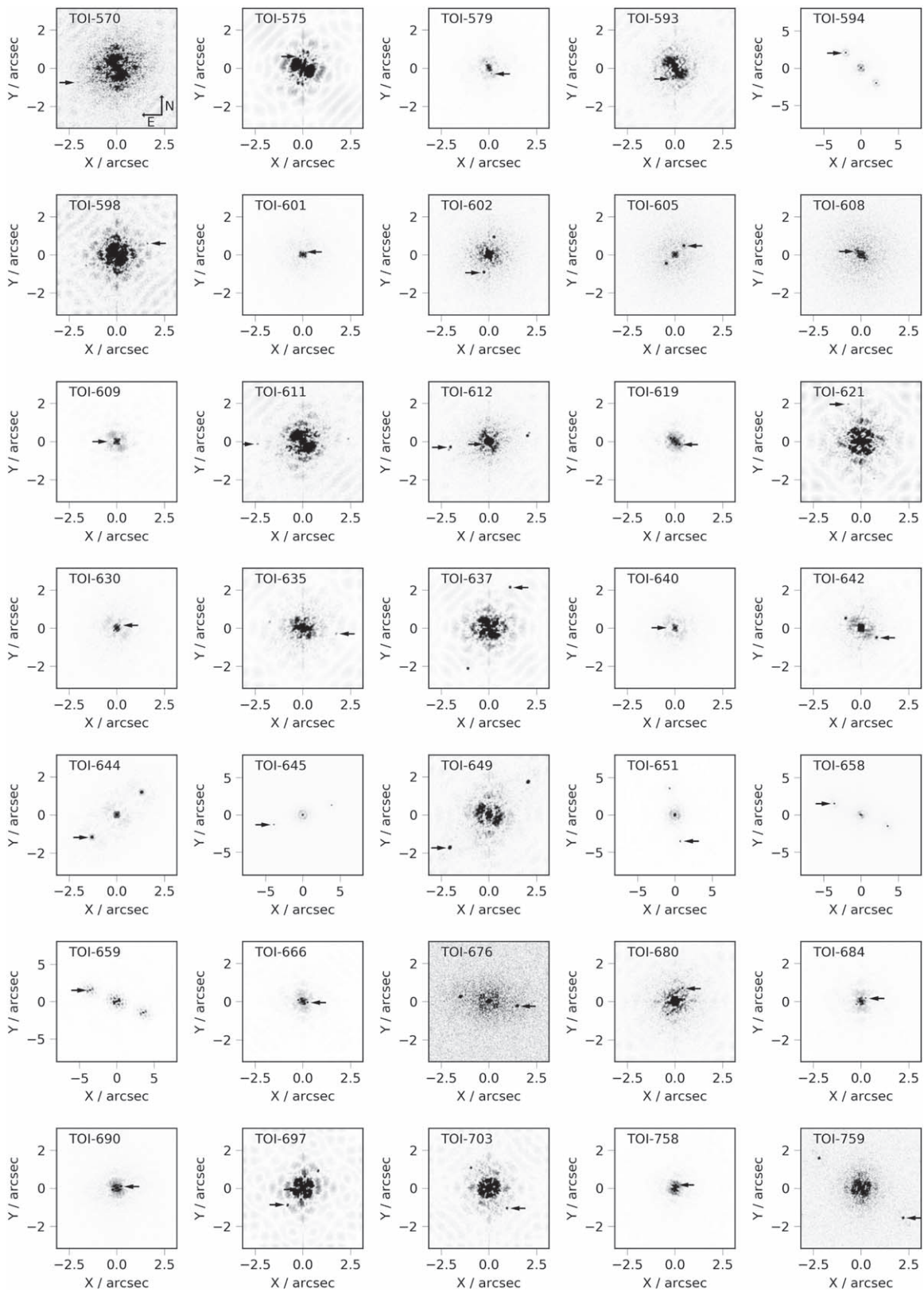


Figure 13. Similar to Figure 11.

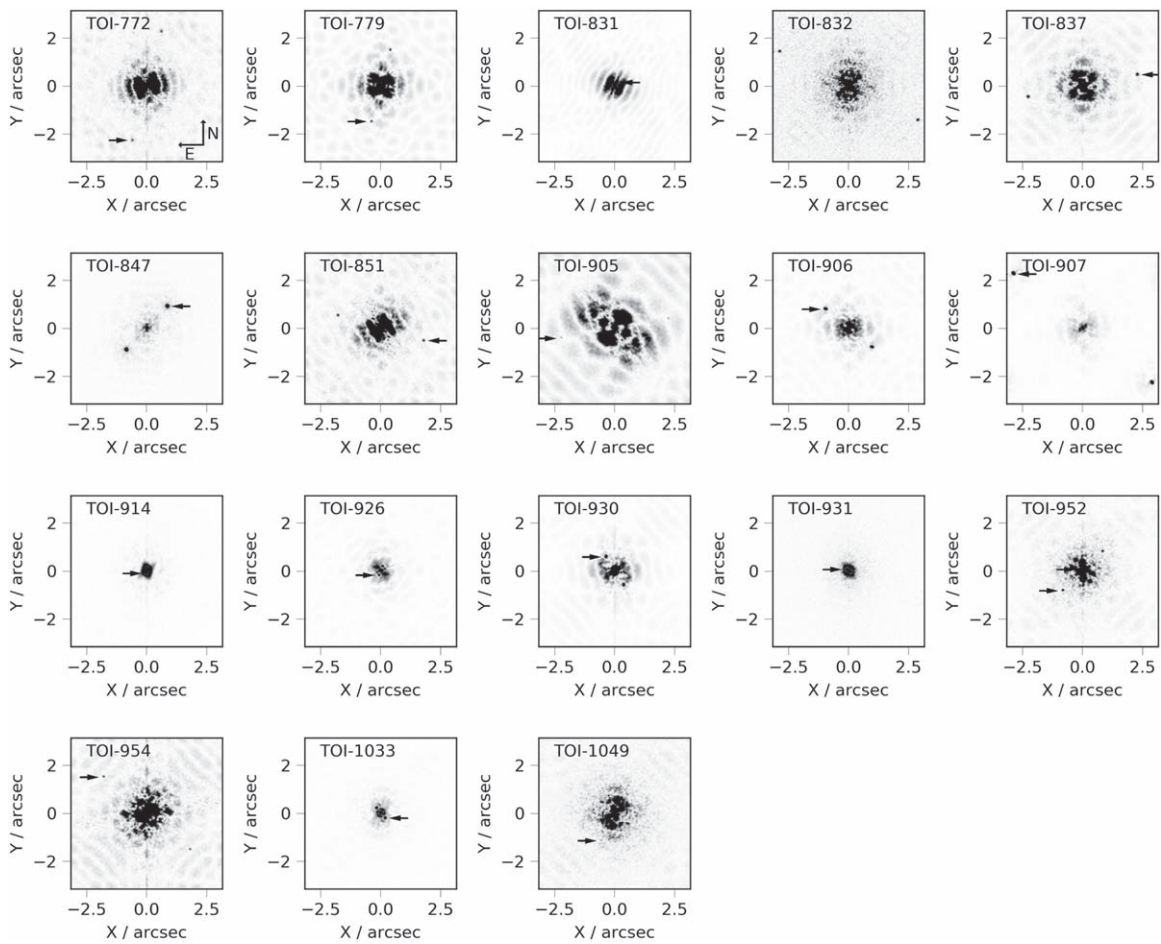


Figure 14. Similar to Figure 11.

Table 2
TIC Matches to Resolved Binaries Detected by SOAR

TOI	TIC Primary	TIC Secondary	SOAR			TIC		
			Sep. (arcsec)	P.A. (deg)	Contrast (mag)	Sep. (arcsec)	P.A. (deg)	Contrast (mag)
(1)	(2)	(3)	(4)	(5)	(6)	(7)	(8)	(9)
123	290131778	1992266045	1.2894	294.6	1.8	1.37	292.2	1.66
128	391949880	675054894	2.2195	153.8	2.4	2.17	153.2	2.51
147	220435095	685140266	2.6583	217.6	4.6	2.65	217.8	4.81
149	260985861	675057530	1.117	132.6	0.1	0.73	132.0	0.82
167	149990841	737110430	0.1593	306.6	0.8	0.39	126.0	0.06
180	51912829	615712419	1.2682	63.7	4.3	1.69	60.8	4.15
240	101948569	616347276	2.3656	197.6	3.1	2.3	197.7	3.19
253	322063810	616169972	2.6623	351.2	4.0	2.58	353.9	3.82
258	350445771	734530071	2.0749	343.2	2.9	2.07	343.5	2.93
343	66497310	2052060639	2.8471	321.0	4.5	2.68	321.0	4.93
386	238059180	767048826	1.1739	274.4	3.5	1.21	276.1	3.21
387	92359850	651667037	2.2878	342.9	3.2	2.28	341.9	3.45
427	70914192	686486697	2.6122	152.9	4.8	2.62	152.6	4.95
433	188989177	188989178	4.0098	324.5	2.9	3.98	324.0	2.85
498	121338379	803532221	2.1845	251.5	3.5	2.62	259.0	3.42
594	146406806	824851862	2.8688	45.3	0.4	2.47	46.0	0.75
611	154459165	831946954	2.3787	93.3	5.5	1.93	105.0	5.83
637	133334108	821927265	2.3926	332.9	5.1	2.41	330.4	5.02
645	157568289	157568287	4.0745	109.0	1.9	4.07	108.9	1.88
651	293689267	293689266	3.2615	219.3	1.5	3.68	39.3	-0.47

Table 2
(Continued)

TOI	TIC Primary	TIC Secondary	SOAR			TIC		
			Sep. (arcsec)	P.A. (deg)	Contrast (mag)	Sep. (arcsec)	P.A. (deg)	Contrast (mag)
(1)	(2)	(3)	(4)	(5)	(6)	(7)	(8)	(9)
658	48476907	48476908	3.88	67.2	0.7	3.87	68.4	0.71
659	48476908	48476907	3.8774	67.2	1.0	3.87	248.4	-0.71
676	219187649	901927162	1.5023	260.6	1.5	1.5	261.2	1.9
759	152147232	942050885	2.694	234.6	3.6	2.69	236.0	3.56
772	286864983	951863424	2.3419	165.3	5.8	2.45	176.9	5.84
837	460205581	847769574	2.3128	281.7	4.6	2.31	280.9	4.7
851	40083958	610472559	1.8583	253.8	5.2	1.92	253.1	5.59
847	231289421	650780404	1.2446	317.1	0.7	0.85	320.9	1.09
905	261867566	1105898342	2.2757	100.8	5.9	2.14	101.5	6.21
907	305424003	1510534043	3.6665	52.0	1.1	3.64	52.1	1.0

Note. Column (1) is the TOI number. Columns (2) and (3) are the TIC number for the primary and secondary stars. Columns (4)–(6) give the measured separation, position angle, and I -band contrast from the SOAR observations. Columns (7)–(9) give the separation and position angle for the system derived from the TIC coordinates and the *TESS* band contrast for each pair of stars.

Table 3
Detection Bias of *TESS* Planets in Multiple Star Systems

TOI	Period (days)	R_P (R_\oplus)	R_* (R_\odot)	Duration (hr)	Depth (ppm)	CDPP _{eff} (ppm)	Sectors	α
(1)	(2)	(3)	(4)	(5)	(6)	(7)	(8)	(9)
101	1.43	13.15	0.89	1.64	20452	597.0	1	1.0
109	2.77	11.66	0.98	2.57	15691	822.2	1	1.0
112	2.5	14.84	1.14	2.88	15044	277.6	4	1.0
114	3.29	10.84	1.24	3.41	7125	148.2	6	1.0
118	6.04	4.93	1.05	2.12	1704	97.0	1	1.0
119	5.54	2.47	0.82	3.03	625	84.5	6	1.0
120	11.54	12.22	2.34	8.56	2389	25.7	1	1.0
121	14.78	14.78	1.23	5.45	14107	84.2	1	1.0
122	5.08	2.39	0.33	1.16	6501	1104.9	1	1.0
124	1.84	7.1	4.09	1.72	2469	275.2	2	1.0

Note. Column (1) is the TOI number. Columns (2) and (3) give the period and radius of the planet with the highest S/N. Column (4) gives the stellar radius from the TIC of the primary star. Columns (5) and (6) give the transit duration and depth from the *TESS* light curves. Column (7) gives the effective combined differential photometric precision, estimated from the photometric precision model of Stassun et al. (2019) and interpolated to the duration of the transit. Column (8) is the number of *TESS* sectors in which the target was observed. Column (9) is the correction factor for the bias against planet detection in binary stars. The factor ranges from zero to 1, with 1 indicating a 100% detection rate even with the flux contamination from a companion star.

(This table is available in its entirety in machine-readable form.)

Table 4
Gaia DR2 Matches to Resolved Binaries Detected by SOAR

TOI	TIC	<i>Gaia</i> DR2 IDs		SOAR			<i>Gaia</i> DR2		
		Primary	Secondary	Sep. (arcsec)	P.A. (deg)	Contrast (mag)	Sep. (arcsec)	P.A. (deg)	Contrast (mag)
(1)	(2)	(3)	(4)	(5)	(6)	(7)	(8)	(9)	(10)
123	290131778	6790773586275235200	6790773586276283648	1.2894	294.6	1.8	1.299	294.18	1.74
128	391949880	4621607053580909568	4621606297664620544	2.2195	153.8	2.4	2.2	153.78	2.55
147	220435095	4762555785607165824	4762555785606163712	2.6583	217.6	4.6	2.642	217.78	4.73
149	260985861	4621665155898448768	4621665155896340480	1.117	132.6	0.1	1.112	132.92	0.1
165	350743714	4765618612685018368	4765618681404494976	2.4855	254.5	0.8	2.476	254.49	0.81
180	51912829	4704412128965720448	4704412133261234176	1.2682	63.7	4.3	1.259	63.1	4.21
240	101948569	4982951791883929472	4982951791883929600	2.3656	197.6	3.1	2.347	197.72	3.44
245	154618248	6554931361478622976	6554931365773693952	1.6268	258.2	1.7	1.623	258.11	1.93
253	322063810	4928367189956040960	4928367189957786240	2.6623	351.2	4.0	2.639	351.78	4.13
258	350445771	4766550723668101376	4766550723668101248	2.0749	343.2	2.9	2.069	343.33	3.03
268	219253008	4779340346001388160	4779340277281911168	2.3025	51.2	0.3	2.29	51.36	0.2
343	66497310	2390762797648110336	2390762797648110208	2.8471	321.0	4.5	2.831	318.96	4.92
386	238059180	5497685201192526976	5497685205489860864	1.1739	274.4	3.5	1.151	268.65	3.54
387	92359850	5101513745613343232	5101513745612593536	2.2878	342.9	3.2	2.285	342.79	3.53
394	9858404	5167486711022397696	5167486711021821568	3.2284	220.2	3.8	3.221	219.92	3.59
427	70914192	5093541152441483008	5093541152441482880	2.6122	152.9	4.8	2.61	152.86	5.27
433	188989177	2983552564639203584	2983552603294316800	4.0098	324.5	2.9	3.984	324.61	3.13
494	19519368	3063507748837064064	3063507744545211264	2.2257	153.7	5.7	2.137	163.16	5.32
498	121338379	3071584413361857280	3071584417656749440	2.1845	251.5	3.5	2.251	252.84	3.52
594	146406806	5548005695180852352	5548005695180850816	2.8688	45.3	0.4	2.868	45.24	0.39
611	154459165	5693753348782558336	5693753348782877440	2.3787	93.3	5.5	2.378	93.73	5.67
635	286132427	3825847092208384640	3825847092207940736	1.7656	260.4	4.8	1.721	252.13	4.93
637	133334108	5537925196465380864	5537925200762994304	2.3926	332.9	5.1	2.393	332.43	5.02
644	63303499	2921445417696098944	2921445417696099072	1.758	132.4	0.4	1.753	132.52	0.39
645	157568289	5566329915436684672	5566329915435059712	4.0745	109.0	1.9	4.068	108.89	1.94
651	72090501	3004190986305089536	3004190986305090176	3.608	191.7	2.2	3.602	191.28	2.59
651	293689267	5568872394338114560	5568872398635858816	3.2615	219.3	1.5	3.344	219.25	1.58
658	48476907	5434682330226436480	5434682330226436736	3.88	67.2	0.7	3.877	67.14	0.75
659	48476908	5434682330226436480	5434682330226436736	3.8774	67.2	1.0	3.877	67.14	0.75
703	237928815	4680955147898508032	4680955152194431616	1.4153	221.8	4.7	1.415	221.71	5.0
759	152147232	5395959695358663296	5395959695358663040	2.694	234.6	3.6	2.687	234.81	3.75
772	286864983	3502914269362946688	3502914273658344448	2.3419	165.3	5.8	2.343	165.32	5.71
837	460205581	5251470948229949568	5251470948222139904	2.3128	281.7	4.6	2.312	281.52	4.7
847	231289421	4741068682700581376	4741068682699441280	1.2446	317.1	0.7	1.238	317.09	0.7
851	40083958	2426349694072115968	2426349694072132608	1.8583	253.8	5.2	1.849	253.86	5.52
905	261867566	5795534040654879744	5795534040654879488	2.2757	100.8	5.9	2.248	100.34	6.13
906	298372701	5984166216846046208	5984166221141887232	1.246	50.8	2.8	1.244	50.4	3.05
907	305424003	5910312231273215872	5910312231273215616	3.6665	52.0	1.1	3.648	52.0	1.11

Note. Column (1) is the TOI number, and column (2) is the TIC number. Columns (3) and (4) are the *Gaia* DR2 source ID for the primary and secondary stars. Columns (5)–(7) give the measured separation, position angle, and *I*-band contrast from the SOAR observations. Columns (8)–(10) give the separation and position angle for the system derived from the *Gaia* DR2 coordinates and the *Gaia* *G*-band contrast for each pair of stars.

Table 5
Gaia DR2 Binaries to *TESS* Targets Not Detected by SOAR

TOI	TIC	<i>Gaia</i> DR2 ID		Distance		Proper Motion		Sep.	Projected Sep.	<i>Gaia</i> Contrast
		Primary	Secondary	Primary	Secondary	Primary	Secondary			
(1)	(2)	(3)	(4)	(5)	(6)	(7)	(8)	(9)	(10)	(11)
				(pc)	(pc)	(mas yr ⁻¹)	(mas yr ⁻¹)	(arcsec)	(au)	(mag)
129	201248411	4923860051276772608	4923860051276772480	61.8	61.9	215.1	219.7	3.81	235.5	4.8
130	263003176	4617759514501503616	4617759518796452608	57.6	56.1	142.7	151.4	2.25	129.6	5.42
143	25375553	6813902839862151936	6813902839862983296	298.1	293.1	13.6	14.3	5.03	1499.4	5.02
174	425997655	4674216245427964416	4674216245427964672	39.0	39.2	111.6	111.5	9.57	373.2	6.45
183	183979262	4686544382117423488	4686544382117422720	213.0	215.4	79.4	80.4	3.21	683.7	2.63
199	309792357	4762582895440787712	4762582861080613248	102.3	101.8	74.2	73.4	9.99	1022.0	7.84
200	410214986	6387058411482257536	6387058411482257280	44.1	44.1	104.2	102.0	5.36	236.4	1.08
204	281781375	4903786336207800576	4903786336207800704	95.3	95.1	173.5	174.0	10.25	976.8	1.16
222	144440290	6531037981670835584	6531037981670835456	84.0	81.1	178.5	177.4	3.46	290.6	8.02
229	120610833	2308834780352875904	2308834784647991168	211.2	233.7	70.7	70.5	4.37	922.9	6.96
248	201793781	4743138925656526976	4743138925656526848	76.0	75.7	94.4	95.6	5.02	381.5	5.45
268	219253008	4779340346001388160	4779341750455118720	320.5	325.9	21.5	21.1	9.99	3201.8	8.13
277	439456714	2353440974955205504	2353440974955205632	64.7	64.7	273.5	274.6	17.25	1116.1	0.3
300	166697854	4743406244421179264	4743406244421179136	397.4	377.7	15.2	16.0	4.1	1629.3	4.66
354	100097716	4959658534969336320	4959658534969336576	366.8	404.5	28.6	28.5	4.84	1775.3	0.65
354	299780329	4632142191744789888	4632142196040368896	305.6	306.9	17.2	17.2	7.37	2252.3	3.25
368	77031413	2323985539482908416	2323985535188372480	233.0	233.6	88.4	87.9	6.12	1426.0	0.59
377	139285736	6529468772420035712	6529468772420035584	244.3	259.0	12.0	10.4	9.29	2269.5	3.14
381	207084429	4917040330405933824	4917040330405933952	75.5	82.3	152.9	156.8	4.94	373.0	7.62
390	250386181	2491782421314919040	2491782417019596160	167.3	171.3	38.4	38.2	6.28	1050.6	6.32
393	29960109	5157183324996790272	5157183324996789760	37.9	37.9	170.6	180.2	8.35	316.5	0.29
396	178155732	5064574720469473792	5064574724768583168	32.0	30.9	162.4	173.2	8.36	267.5	9.8
397	219379012	4785828357959075840	4785828357959076480	167.0	168.4	31.3	29.8	4.32	721.4	4.84
412	7624182	4844367147295252864	4844365669826503808	460.7	446.6	11.5	11.3	7.88	3630.3	6.0
414	325680697	5171630735987857152	5171630735987104512	115.1	114.8	48.3	48.6	4.5	517.9	5.25
426	189013224	2983316311375470976	2983316311375257472	113.6	112.6	26.2	27.8	8.88	1008.8	0.77
440	143350972	2971536418673198976	2971536418671276544	49.3	49.1	113.0	112.1	6.45	318.0	4.87
441	316916655	2987545475475708416	2987545548491503360	184.0	177.7	10.9	12.3	15.64	2877.8	6.0
470	37770169	2912264564319611136	2912264564316598272	130.5	130.1	85.1	84.4	13.6	1774.8	6.25
470	37770169	2912264564319611136	2912264564316598144	130.5	130.5	85.1	86.4	13.74	1793.1	5.89
498	121338379	3071584413361857280	3071584417656748928	188.4	176.6	23.4	21.7	5.2	979.7	7.25
505	268644785	5489780919480009472	5489780919477609600	324.7	315.8	5.1	5.4	6.09	1977.4	6.65
510	238086647	5508330367833229824	5508330367831469952	93.1	94.0	124.6	122.8	5.48	510.2	3.93
575	386435344	5709861464697757824	5709861468994311424	182.0	156.4	48.6	48.5	5.36	975.5	8.28
580	81419525	5519619186857962112	5519619191155977344	346.5	475.4	11.6	9.1	14.09	4882.2	10.99
581	180987952	5525188767305211904	5525188728649771392	434.2	428.8	13.6	20.8	7.8	3386.8	8.56
592	196286587	5695996352497664512	5695996348197148032	358.4	385.6	8.6	33.0	11.28	4042.8	1.49
638	78154865	3822912388299321728	3822912392594624128	96.6	97.6	14.3	16.0	10.53	1017.2	4.32
648	78672342	2933433564771909888	2933433564771909760	637.3	814.6	11.0	11.6	2.95	1880.0	5.9
650	349373192	5293295919554813952	5293296130007438848	402.8	348.7	12.6	12.9	8.97	3613.1	8.93
670	147660201	5388433503908280320	5388433503908279168	191.5	183.6	57.9	56.4	13.79	2640.8	1.91
708	391821647	4657888149862830720	4657888150116259584	214.8	347.2	24.0	21.4	13.74	2951.4	9.36
756	73649615	6129327525817451648	6129327319659021056	86.2	86.2	218.3	217.6	11.09	956.0	1.35
764	181159386	5385762893242980992	5385762824520652160	789.3	754.5	6.5	6.4	5.96	4704.2	6.21

Table 5
(Continued)

TOI	TIC	<i>Gaia</i> DR2 ID		Distance		Proper Motion		Sep.	Projected Sep.	<i>Gaia</i> Contrast
		Primary (3)	Secondary (4)	Primary (5)	Secondary (6)	Primary (7)	Secondary (8)			
811	100757807	2890519660294945920	2890519660294833792	284.0	283.8	29.7	29.1	4.33	1229.7	1.83
815	102840239	5415648821879172096	5415648821874435584	59.7	59.3	11.4	12.3	6.04	360.6	2.48
824	193641523	5880886001621564928	5880886001577333888	63.9	69.2	160.9	3.3	6.7	428.1	9.16
829	276128561	6199033466340798464	6199033466344807040	142.5	138.8	71.0	71.4	5.46	778.0	5.28
832	350332997	4768613025228556416	4768613029524059648	586.7	617.2	13.7	12.9	3.7	2170.8	4.76
858	198008005	4683737294568479104	4683737294569921664	255.8	250.5	15.1	15.5	10.95	2801.0	0.28
878	219380235	4771537902252716416	4771537897957355392	334.5	324.6	35.5	34.9	5.64	1886.6	6.49
915	259389219	4781316164099781760	4781316168396825728	506.4	443.0	10.1	29.7	6.05	3063.7	4.18
938	332660150	3189432444744896512	3189432444743495936	215.0	195.0	12.6	12.9	7.95	1709.2	7.6

Note. Column (1) is the TOI number, and column (2) is the TIC number. Columns (3) and (4) are the TIC number for the primary and secondary stars. Columns (5) and (6) give the distance from the star from Bailer-Jones et al. (2018). Columns (7) and (8) give the proper motion in *Gaia* DR2 for the primary and secondary stars. Column (9) gives the on-sky separation based on the *Gaia* DR2 coordinates, and Column (10) gives the projected physical separation using the average of the distances to the two stars. Column (11) gives the *Gaia* *G*-band contrast of the stellar pair.

Table 6
Full SOAR Speckle Observation List and Binary Properties

TOI	TIC	Comp.	R.A., Decl. (J2000)		Filter	Obs. Year	θ (deg)	$\rho * \sigma_\theta$ (mas)	ρ (arcsec)	σ_ρ (mas)	Δm (mag)	Flag	Min. ρ (arcsec)	Limiting Δm	
			(deg)	(deg)										0''15 (15)	1'' (16)
(1)	(2)	(3)	(4)	(5)	(6)	(7)	(8)	(9)	(10)	(11)	(12)	(13)	(14)	(15)	(16)
101	231663901	...	318.73713	-55.87186	<i>I</i>	2018.731							0.067	2.20	2.97
109	29344935	...	313.21605	-25.68764	<i>I</i>	2019.375						:	0.098	0.00	0.00
112	388104525	...	55.93345	-65.19383	<i>I</i>	2019.534							0.064	2.33	3.88
114	25155310	...	63.37440	-69.22675	<i>I</i>	2019.534							0.064	2.51	4.37
118	266980320	...	349.56216	-56.90408	<i>I</i>	2018.731							0.048	3.00	4.05
119	278683844	...	99.23777	-58.01477	<i>I</i>	2018.732							0.048	2.36	3.72
120	394137592	...	4.44608	-66.35889	<i>I</i>	2018.731							0.043	2.57	3.82
121	207081058	...	331.86741	-41.81472	<i>I</i>	2018.731							0.052	2.33	3.67
122	231702397	...	332.94818	-58.94689	<i>I</i>	2018.975							0.041	1.68	3.86
123	290131778	AB	319.69946	-26.61611	<i>I</i>	2018.731	294.6	0.2	1.289	0.2	1.8	*	0.041	2.42	4.38

Note. Columns (1) and (2) give the TOI and TIC numbers, respectively. Column (3) designates the components of the resolved binaries according to the WDS style (mostly “AB”). This matters for resolved triple systems, indicating their hierarchy. The equatorial coordinates for J2000, in degrees, are given in columns (4) and (5). Column (6) gives the filter (mostly *I*, with a few targets also observed in *V*), and Column (7) gives the date of the observation (in Julian years). For resolved binaries, Columns (8) and (10) give the position angle θ and separation ρ , while Columns (9) and (11) contain estimates of the measurement errors in tangential ($\rho * \sigma_\theta$) and radial (σ_ρ) directions in mas. The measured magnitude difference Δm is given in Column (12). Some targets have multiple measurements. For unresolved sources (single stars), Columns (8)–(12) are empty. Flags for the photometry are provided in column (13). These flags are “:” for a companion with a low S/N, “q” for an identified quadrant from the SAA images, and “*” if the photometry is corrected for anisoplanatism using the average image. The estimated resolution limit is listed in column (14) for all stars; columns (15) and (16) give the estimated maximum detectable Δm at separations of 0''.15 and 1''.

(This table is available in its entirety in machine-readable form.)

ORCID iDs

Carl Ziegler  <https://orcid.org/0000-0002-0619-7639>
 Andrei Tokovinin  <https://orcid.org/0000-0002-2084-0782>
 Nicholas Law  <https://orcid.org/0000-0001-9380-6457>
 Andrew W. Mann  <https://orcid.org/0000-0003-3654-1602>

References

- Alexander, R. 2012, *ApJL*, **757**, L29
 Arenou, F., Luri, X., Babusiaux, C., et al. 2018, *A&A*, **616**, A17
 Astropy Collaboration, Robitaille, T. P., Tollerud, E. J., et al. 2013, *A&A*, **558**, A33
 Bailer-Jones, C. A. L., Rybizki, J., Fousneau, M., Mantelet, G., & Andrae, R. 2018, *AJ*, **156**, 58
 Bakos, G. Á 2018, in *Handbook of Exoplanets*, ed. H. J. Deeg & J. A. Belmonte (Cham: Springer), 111
 Baranec, C., Riddle, R., Law, N. M., et al. 2014, *ApJL*, **790**, L8
 Baranec, C., Riddle, R., & Law, N. M. 2017, arXiv:1709.07103
 Baranec, C., Ziegler, C., Law, N. M., et al. 2016, *AJ*, **152**, 18
 Borucki, W. J., Koch, D., Basri, G., et al. 2010, *Sci*, **327**, 977
 Bouma, L. G., Masuda, K., & Winn, J. N. 2018, *AJ*, **155**, 244
 Bowler, B. P. 2016, *PASP*, **128**, 102001
 Carrera, D., Johansen, A., & Davies, M. B. 2015, *A&A*, **579**, A43
 Ciardi, D. R., Beichman, C. A., Horch, E. P., & Howell, S. B. 2015, *ApJ*, **805**, 16
 Ciardi, D. R., Fabrycky, D. C., Ford, E. B., et al. 2013, *ApJ*, **763**, 41
 Davies, M. B., Adams, F. C., Armitage, P., et al. 2014, in *Protostars and Planets VI*, ed. H. Beuther et al. (Tucson, AZ: Univ. Arizona Press), 787
 Deacon, N. R., Kraus, A. L., Mann, A. W., et al. 2016, *MNRAS*, **455**, 4212
 Dong, R., Hall, C., Rice, K., & Chiang, E. 2015, *ApJL*, **812**, L32
 Dotter, A., Chaboyer, B., Jevremović, D., et al. 2008, *ApJS*, **178**, 89
 Dragomir, D., Teske, J., Günther, M. N., et al. 2019, *ApJL*, **875**, L7
 Dressing, C. D., & Charbonneau, D. 2013, *ApJ*, **767**, 95
 El-Badry, K., & Rix, H.-W. 2018, *MNRAS*, **480**, 4884
 Espinoza, N., Brahm, R., Henning, T., et al. 2019, arXiv:1903.07694
 Evans, D. F., Southworth, J., Maxted, P. F. L., et al. 2016, *A&A*, **589**, A58
 Evans, D. F., Southworth, J., Smalley, B., et al. 2018, *A&A*, **610**, A20
 Fabrycky, D., & Tremaine, S. 2007, *ApJ*, **669**, 1298
 Feiden, G. A., & Chaboyer, B. 2012, *ApJ*, **757**, 42
 Fontanive, C., Rice, K., Bonavita, M., et al. 2019, *MNRAS*, **485**, 4967
 Ford, E. B., & Rasio, F. A. 2008, *ApJ*, **686**, 621
 Foreman-Mackey, D. 2016, *JOSS*, **1**, 24
 Foreman-Mackey, D., Hogg, D. W., Lang, D., & Goodman, J. 2013, *PASP*, **125**, 306
 Fressin, F., Torres, G., Charbonneau, D., et al. 2013, *ApJ*, **766**, 81
 Gaia Collaboration, Brown, A. G. A., Vallenari, A., et al. 2018, *A&A*, **616**, A1
 Gaia Collaboration, Prusti, T., de Bruijne, J. H. J., et al. 2016, *A&A*, **595**, A1
 Gaidos, E., Mann, A. W., Kraus, A. L., & Ireland, M. 2016, *MNRAS*, **457**, 2877
 Hamers, A. S. 2017, *ApJL*, **835**, L24
 Henden, A. A., Welch, D. L., Terrell, D., & Levine, S. E. 2009, AAS Meeting Abstracts, **214**, 407.02
 Hirsch, L. A., Ciardi, D. R., Howard, A. W., et al. 2017, *AJ*, **153**, 117
 Holman, M., Touma, J., & Tremaine, S. 1997, *Natur*, **386**, 254
 Horch, E. P., Howell, S. B., Everett, M. E., & Ciardi, D. R. 2014, *ApJ*, **795**, 60
 Howard, A. W., Marcy, G. W., Bryson, S. T., et al. 2012, *ApJS*, **201**, 15
 Huang, C., Wu, Y., & Triaud, A. H. M. J. 2016, *ApJ*, **825**, 98
 Huang, C. X., Burt, J., Vanderburg, A., et al. 2018, *ApJL*, **868**, L39
 Jackson, B. K., Barnes, R., & Greenberg, R. 2009, *ApJ*, **698**, 1357
 Jang-Condell, H., Mugrauer, M., & Schmidt, T. 2008, *ApJL*, **683**, L191
 Jenkins, J. M., Twicken, J. D., McCauliff, S., et al. 2016, *Proc. SPIE*, **9913**, 99133E
 Jones, M. I., Brahm, R., Espinoza, N., et al. 2019, *A&A*, **625**, A16
 Jurić, M., & Tremaine, S. 2008, *ApJ*, **686**, 603
 Knutson, H. A., Fulton, B. J., Montet, B. T., et al. 2014, *ApJ*, **785**, 126
 Kraus, A. L., & Hillenbrand, L. A. 2007, *AJ*, **134**, 2340
 Kraus, A. L., Ireland, M. J., Hillenbrand, L. A., & Martinache, F. 2012, *ApJ*, **745**, 19
 Kraus, A. L., Ireland, M. J., Huber, D., Mann, A. W., & Dupuy, T. J. 2016, *AJ*, **152**, 8
 Law, N. M., Morton, T., Baranec, C., et al. 2014, *ApJ*, **791**, 35
 Lissauer, J. J., Fabrycky, D. C., Ford, E. B., et al. 2011, *Natur*, **470**, 53
 Mann, A. W., Dupuy, T., Kraus, A. L., et al. 2019, *ApJ*, **871**, 63
 Matson, R. A., Howell, S. B., Horch, E. P., & Everett, M. E. 2018, *AJ*, **156**, 31
 Matsumura, S., Ida, S., & Nagasawa, M. 2013, *ApJ*, **767**, 129
 Mordasini, C., Alibert, Y., Benz, W., Klahr, H., & Henning, T. 2012, *A&A*, **541**, A97
 Morton, T. D., Bryson, S. T., Coughlin, J. L., et al. 2016, *ApJ*, **822**, 86
 Morton, T. D., & Johnson, J. A. 2011, *ApJ*, **738**, 170
 Naoz, S., Farr, W. M., Lithwick, Y., Rasio, F. A., & Teysandier, J. 2011, *Natur*, **473**, 187
 Naoz, S., Farr, W. M., & Rasio, F. A. 2012, *ApJL*, **754**, L36
 Ngo, H., Knutson, H. A., Hinkley, S., et al. 2015, *ApJ*, **800**, 138
 Ngo, H., Knutson, H. A., Hinkley, S., et al. 2016, *ApJ*, **827**, 8
 Pecaut, M. J., Mamajek, E. E., & Bubar, E. J. 2012, *ApJ*, **746**, 154
 Price-Whelan, A. M., Sipőcz, B. M., Günther, H. M., et al. 2018, *AJ*, **156**, 123
 Quinn, S. N., Becker, J. C., Rodriguez, J. E., et al. 2019, *AJ*, **158**, 177
 Quintana, E. V., Adams, F. C., Lissauer, J. J., & Chambers, J. E. 2007, *ApJ*, **660**, 807
 Raghavan, D., McAlister, H. A., Henry, T. J., et al. 2010, *ApJS*, **190**, 1
 Raymond, S. N., Armitage, P. J., Moro-Martín, A., et al. 2011, *A&A*, **530**, A62
 Ricker, G. R., Winn, J. N., Vanderspek, R., et al. 2014, *Proc. SPIE*, **9143**, 914320
 Rodriguez, J. E., Quinn, S. N., Huang, C. X., et al. 2019, *AJ*, **157**, 191
 Schmidt, M. 1968, *ApJ*, **151**, 393
 Skrutskie, M. F., Cutri, R. M., Stiening, R., et al. 2006, *AJ*, **131**, 1163
 Stassun, K. G., Oelkers, R. J., Paegert, M., et al. 2019, *AJ*, **158**, 138
 Stassun, K. G., Oelkers, R. J., Pepper, J., et al. 2018, *AJ*, **156**, 102
 Street, R. A., Pollaco, D. L., Fitzsimmons, A., et al. 2003, in *ASP Conf. Ser.* 294, *Scientific Frontiers in Research on Extrasolar Planets*, ed. D. Deming & S. Seager (San Francisco, CA: ASP), 405
 Takeda, G., Kita, R., & Rasio, F. A. 2008, *ApJ*, **683**, 1063
 Tokovinin, A. 2018, *PASP*, **130**, 035002
 Tokovinin, A., Mason, B. D., & Hartkopf, W. I. 2010, *AJ*, **139**, 743
 Torres, G., Fressin, F., Batalha, N. M., et al. 2011, *ApJ*, **727**, 24
 Triaud, A. H. M. J., Martin, D. V., Ségransan, D., et al. 2017, *A&A*, **608**, A129
 Vanderburg, A., Huang, C. X., Rodriguez, J. E., et al. 2019, *ApJL*, **881**, L19
 Veras, D., & Armitage, P. J. 2006, *ApJ*, **645**, 1509
 Wang, J., Fischer, D. A., Xie, J.-W., & Ciardi, D. R. 2015, *ApJ*, **813**, 130
 Welsh, W. F., Orosz, J. A., Carter, J. A., et al. 2012, *Natur*, **481**, 475
 Winters, J. G., Henry, T. J., Jao, W.-C., et al. 2019, *AJ*, **157**, 216
 Wizinowich, P. L., Le Mignant, D., Bouchez, A. H., et al. 2006, *PASP*, **118**, 297
 Wu, Y., Murray, N. W., & Ramsahai, J. M. 2007, *ApJ*, **670**, 820
 Xie, J.-W., Dong, S., Zhu, Z., et al. 2016, *PNAS*, **113**, 11431
 Ziegler, C., Law, N. M., Baranec, C., et al. 2018a, *AJ*, **156**, 259
 Ziegler, C., Law, N. M., Baranec, C., et al. 2018b, *AJ*, **155**, 161
 Ziegler, C., Law, N. M., Baranec, C., et al. 2018c, *AJ*, **156**, 83
 Ziegler, C., Law, N. M., Morton, T., et al. 2017, *AJ*, **153**, 66